Phys Chem Minerals (2001) 28: 641–664

ORIGINAL PAPER

B. H. Tan · I. Jackson · J. D. Fitz Gerald

High-temperature viscoelasticity of fine-grained polycrystalline olivine

Received: 29 September 2000 / Accepted: 7 May 2001

Abstract Torsional forced-oscillation and microcreep methods have been employed in a study of the viscoelastic behaviour of fine-grained polycrystalline olivine at high temperatures (to 1300 °C), seismic frequencies and low strain amplitudes. The Fo_{90} specimens are of low porosity and low dislocation density. They vary in mean grain size from 8 to 150 μm and contain only trace amounts ($\ll$0.1 vol%) of quenched melt glass. For $T \leq 900$ °C, their behaviour is essentially elastic and the shear modulus G closely approaches that expected for a dense polycrystal from single-crystal elasticity data – confirming the suppression of thermal microcracking in this study. At higher temperatures, pronounced absorption-band dissipation and associated dispersion of the shear modulus provide evidence of linear viscoelastic behaviour. Both recoverable (anelastic) and permanent (viscous) strains are involved and the proportion of the latter increases with increasing temperature and decreasing frequency. Comparison of the results for the three specimens provides a clear indication that the viscoelastic behaviour, attributed to diffusional processes, is grain-size-sensitive with the dissipation and associated dispersion increasing with decreasing grain size. Both elastically accommodated and diffusionally accommodated grain-boundary sliding appear to be implicated.

Key words Olivine · Viscoelastic behaviour · Andrade model · Burgers model · Seismic wave attenuation · Anelastic behaviour · Grain boundary · Diffusion

Introduction

The attenuation of seismic waves in the Earth's mantle has been intensively studied since the 1960's. A recent review by Romanowicz and Durek (2000; see also Jackson and Rigden 1998) highlights the following major findings. The dissipation Q^{-1} is associated predominantly with shear deformation (governed by the shear modulus G) rather than hydrostatic compression (described by the bulk modulus K). The radial variation of Q_G^{-1} in the upper mantle and transition zone is relatively well established. The attenuation is most pronounced at depths of about 80–220 km in the upper mantle, where Q^{-1} exceeds 0.01. This zone of strong attenuation is overlain by a low-loss lid, and underlain by a region within which Q^{-1} decreases markedly with increasing depth to values of 0.0025–0.003 in the upper part of the lower mantle. Q_G^{-1} appears to be mildly frequency-dependent, varying as $\omega^{-\alpha}$ with $\alpha \sim 0.1$–0.4.

The upper mantle zone of high attenuation is also characterised by shear wave speeds which are generally relatively low (e.g. Dziewonski and Anderson 1981; Grand and Helmberger 1984) and highly variable laterally (Grand 1994; Zielhuis and Nolet 1994; Su et al. 1994; Ritzwoller and Lavely 1995; Li and Romanowicz 1996; Su and Dziewonski 1997; van der Hilst et al. 1998). Indeed, both the radial models and the superimposed lateral variability revealed by tomographic studies (Durek et al. 1993; Romanowicz 1995) exhibit a strong spatial correlation between high attenuation and relatively low shear wave speeds. This association is suggestive of thermally activated viscoelastic behaviour in the solid state (e.g. Goetze 1977) and, at least locally (e.g. beneath mid-ocean ridges), with the effects of partial melting (e.g. Toomey et al. 1998; Webb and Forsyth 1998).

Interpretation of these seismological observations requires an understanding of the viscoelastic behaviour of ultramafic materials at high temperature and seismic frequency established through laboratory experiments conducted under carefully controlled conditions. The torsional forced-oscillation/microcreep methods best suited to such measurements have been developed and applied to natural ultramafic rocks by Berckhemer et al. (1982) and Jackson et al. (1992). These studies revealed

B. H. Tan · I. Jackson (✉) · J. D. Fitz Gerald
Research School of Earth Sciences,
Australian National University,
Canberra 0200 ACT, Australia
e-mail: Ian.Jackson@anu.edu.au

pronounced dissipation and associated shear modulus dispersion at high subsolidus temperatures, and a frequency dependence of Q^{-1} given by $\omega^{-\alpha}$ with exponent $\alpha \sim 0.1$–0.3.

However, detailed interpretation of the observed behaviour in terms of defect-related relaxation mechanisms was significantly complicated by the occurrence of thermal microcracking, by the progressive dehydration of hydrous layer-silicate minerals, and in the study of Åheim dunite by Berckhemer et al. by melting, which may account for their very high activation energy (800 kJ mol^{-1}). Dissipation has also been measured at high temperatures and seismic frequencies on untreated and predeformed specimens of single-crystal San Carlos olivine (Gueguen et al. 1989). This sensitivity of attenuation to prior deformation (and thus dislocation density), along with the approximate consistency between the results for natural rock specimens and single-crystal olivine, suggest that grain-size-insensitive (dislocation-related) processes may be responsible for the viscoelastic relaxation.

In order to avoid the difficulties arising from the chemical complexity of natural rocks and the inevitable microcracking during thermal cycling of relatively coarse-grained materials, the emphasis has switched in recent studies to fine-grained synthetic ultramafic materials. Tan et al. (1997a) demonstrated the viability of this approach, reporting measurements of the temperature and frequency dependence of both shear modulus G and associated strain energy dissipation Q^{-1} for an Fo_{90} olivine polycrystal of high purity and $\sim$50 μm grain size which was prepared by hot-isostatic pressing of grain-size-sorted powder derived from carefully selected crystals of San Carlos (Arizona) olivine. Subsequently, Gribb and Cooper (1998) reported torsional forced-oscillation and microcreep data for a very fine-grained synthetic dunite produced by hot-isostatic pressing powder obtained by pulverising Balsam Gap (North Carolina) dunite.

Here, we extend the preliminary work of Tan et al. (1997a) by reporting results for a suite of three synthetic olivine polycrystals of varying grain size and microstructure. These specimens remain essentially melt-free and uncracked throughout the 20–1300 °C range of the measurements, and therefore provide a robust subsolidus baseline, at least at relatively small grain size, with which seismological data can eventually be compared.

Experimental method

Specimen preparation

Preparation of pure, grain-size-sorted olivine powders

A suite of San Carlos olivine megacrysts of almost gem quality and 3–5 mm grain size was selected from material purchased from Arizona Gems and Crystals, Safford, Arizona. Crystals containing visible inclusions (typically orthopyroxene, clinopyroxene, chromian spinel and magnetite, and minor hydrous minerals) were avoided. The selected crystals were crushed in a tungsten carbide mill, and then sieved to retrieve the 250–180 μm and 180–125 μm grain-size fractions – these ranges being chosen to allow optimal purification by subsequent heavy liquid and magnetic separation – and by physical removal of individual impurity grains. The fraction of the crushed powder recovered from suspension in methyl iodide (specific gravity 3.3) was significantly depleted in lighter pyroxene and heavier magnetite impurities, the latter being further reduced in concentration by magnetic separation. The residual level of impurities (<1%) was substantially reduced by manual removal of any impurity grains recognised through a binocular microscope.

The purified powder was then ground in an agate mill – the speed and duration of milling being chosen to achieve effective comminution with minimal contamination. The milled powder was passed through a set of brass sieves reserved for use with $Fo_{\sim 90}$ olivine, yielding batches of powder of 38–63 μm and <38-μm particle size. Finally, sedimentation from suspension in ethanol over time intervals of order 1 h, 1 day and 1 month, repeated for the 1-h and 1-day intervals, yielded powders with relatively narrow particle-size distributions of 10–38, 2–10 and <2 μm, respectively.

Cold-pressing and preliminary heat treatment

Pellets of 15 mm diameter and 7–8 mm length, containing $\sim$30% porosity, were produced by cold pressing in a hardened steel die under 300 MPa uniaxial pressure. Prior to hot-pressing (described below), such pellets were either simply oven-dried (150 °C) for several days or prefired at 1200 °C under inert atmosphere to remove strongly adsorbed water and any residues from organic solvents. For temperatures above 700 °C a gas mixture comprising equal partial pressures of CO and CO_2 was used, yielding log f_{O_2} (Pa) ~ -6 at 1200 °C (Muan and Osborn 1965). In order to prevent the precipitation of graphite from gas of this composition (Muan and Osborn 1965), argon was substituted for the CO/CO_2 gas mix for temperatures below 700 °C. The pellets emerge from this treatment cream to pale green in colour.

Hot-isostatic pressing

Dense polycrystalline olivine compacts were prepared from stacks consisting of several cold-pressed pellets by hot-isostatic pressing within an internally heated gas-medium high-pressure apparatus (Paterson 1990). Hot-pressing conditions, optimised through extensive prior exploratory experiments, for the various specimens mechanically tested in this study are displayed in Table 1. The stack of pellets was located between blind alumina pistons within a mild steel tube of 15 mm internal diameter, sealed at either end with an O ring. Thin layers of iron foil inserted at either end of the stack of pellets served to isolate the specimen from the alumina pistons and also to reduce thermal stresses caused during cooling by the mismatch in thermal contraction between the alumina pistons and olivine specimen. The Fe foils and mild steel jacket enclosing the specimen impose a chemical environment that is strongly reducing (Raterron et al. 1998), leading to the precipitation within the olivine polycrystal of some small Ni-rich metallic blebs.

Following transverse sectioning of the steel-jacketed hot-pressed compacts for microstructural characterisation, the steel jackets were removed from the dense hot-pressed olivine compacts either by acid (HNO_3/HCl) dissolution or, on the later-tested specimens (nos. 6261 and 6328), by mechanical grinding. A cylindrical specimen typically 12 mm in diameter and 30 mm in length was then prepared by precision grinding. The specimen was cleaned successively in water, ethanol and acetone and then oven-dried in anticipation of mechanical testing described below.

Microstructural characterisation

Light microscopy

Microstructures were examined by polarised light microscopy in both transmission and reflection. Thin sections were epoxy-

Table 1 Details of Fo_{90} polycrystalline specimens prepared for and tested in this study

Specimen no.	Powder precursor		Hot-pressing conditions			Hot-pressed (HP) and mechanically tested (AT) specimens						Comments
	Grain size, (μm)	Heat treatment	P, MPa	T, °C	t, h	Density g cm^{-3} (HP)	Porosity (%)[a]	Grain size (HP)	Grain size (AT)	$[H_2O]^b$ wt ppm (HP)	$[H_2O]^b$ wt ppm (AT)	
6261	10–38	Oven-dried	300	1300	6	3.305(1)	1.0	25	30[c]	230[d]	130	Texturally well-equilibrated, stable grain size
6268/9	10–38	Prefired 1200 °C 24 h	300	1300	14 (8 + 6)	3.275(1)	1.9	15	15	25[d]	–	Stable bimodal grain-size distribution: small new grains rimming large old grains
6328	2–10	Prefired 1200 °C 24 h	300	1300	4	3.330(1)	0.2	8[e]	150	5	35–70[d,f]	Abnormal grain growth during testing

[a] Based on density of 3.338 g cm^{-3} for natural Fo_{90} olivine (Brown 1980)
[b] Broad-band absorption attributable to free molecular water rather than structurally bound OH; 3400 cm^{-1} absorbance converted into $[H_2O]$ with absorption coefficient of 81 cm^{-1} (mol/l)$^{-1}$ for free water, measured path length and standard density of 3.288 g cm^{-3}
[c] Bench-top ultrasonic wavespeeds (V_P = 6.79 km s^{-1}, V_S = 4.11 km s^{-1}) are much lower than the Hashin–Shtrikman averages (8.35 km s^{-1} and 4.83 km s^{-1}, Isaak 1992) calculated from single-crystal elastic constants, indicating pervasive microcracking
[d] Path length assumed to be 0.0425 cm as for AT6261
[e] Bench-top ultrasonic wavespeeds (V_P = 8.16 km s^{-1}, V_S = 4.96 km s^{-1}) are comparable with Hashin–Shtrikman averages (sec[e]), suggesting minimal crack porosity
[f] Heterogeneity in inferred $[H_2O]$ associated with pervasive microcracking and possible intrusion of adhesives during preparation of section

impregnated, then commonly ground as thin as 10 μm before careful polishing to improve the clarity of observations, particularly for the fine grained materials – such thin sections can be examined using transmitted light microscopy since olivine has relatively high birefringence. Dislocation structures were revealed in some thin sections by oxidative decoration (Kohlstedt et al. 1976). Average grain sizes (Table 1) were measured by the simple linear intercept method (100–200 grains) with average intercept length being multiplied by a shape factor of 1.5 to estimate the average grain size. Estimates of volume fractions of small melt and impurity bodies used reflected light and high-power objectives; area fractions of visible structures were averaged over many tens of fields of view. The largest melt structures (on the order of 10 μm diameter) in coarser-grained materials were readily identified because (1) reflectance of the silicate glass is well below that of surrounding olivine and (2) epoxy (e.g. in pores and cracks) also has low reflectance but is soft and so polishes significantly more roughly than melt glass; it also has a refractive index below that of olivine and glass which is useful in transmitted light. (Some melt presence was also cross-checked with X-ray microanalysis – see below). Using these characteristics, with practice, even near-micrometre-sized melts and impurities could be reliably identified with light microscopy. This was important because the petrographic thin sections provided the best opportunity to examine large and representative areas in a reasonable time.

Electron microscopy

In general, the techniques used for scanning (SEM) and transmission (TEM) electron microscopy and microanalysis were routine. For SEM, polished blocks were examined in a JEOL JSEM6400 at 15 kV with secondary and backscattered imaging and quantitative analysis performed with standard-based correction of X-ray intensities measured by energy-dispersive spectrometry (EDS). For TEM, parts of thin sections were carefully attached to Cu grids and thinned to perforation using Ar ions. TEM was carried out at 300 kV in a Philips EM430 – bright- and dark-field images were used to identify features such as dislocations, melts and metal blebs. Microanalysis using EDS in TEM was conventional although the broad-beam methods of Drury and Fitz Gerald (1996) were applied in carefully searching for impurity segregations at grain boundaries.

Determination of infrared absorbance and [H_2O]

Doubly polished sections of either 100 or 500 μm nominal thickness were prepared for examination by IR spectroscopy. Following acetone dissolution of the resin (crystalbond) used in mounting the sections during their preparation, these were oven-dried pending IR examination. The IR measurements were made on a Bruker IFS 28 with attached microscope, operating under OPUS software. In transmission mode, the absorbance given by $A(\nu) = \log[I_0(\nu)/I(\nu)]$ is determined. I_0 and I are, respectively, the intensities of the incident and transmitted beams, and ν is the wavenumber. The absorbance depends on the thickness of specimen, and the concentration and molar absorption coefficient of the absorbing species. Absorption due to the presence of water appears in the IR spectrum in the wavenumber range of 4000–2000 cm^{-1}, typically for these specimens as a broad band due to molecular water (Fig. 1). Following correction for absorption due to laboratory air and baseline effects, the concentration of molecular (i.e. "free") water as H_2O (wt ppm) was calculated from A (3400 cm^{-1}) with an absorption coefficient of 811 cm^{-1} (mol/l)$^{-1}$ (Thompson 1965; Rossman 1988).

Density determination

The density of each specimen precision-ground for mechanical testing was determined by the Archimedean method involving immersion in ethanol (Table 1).

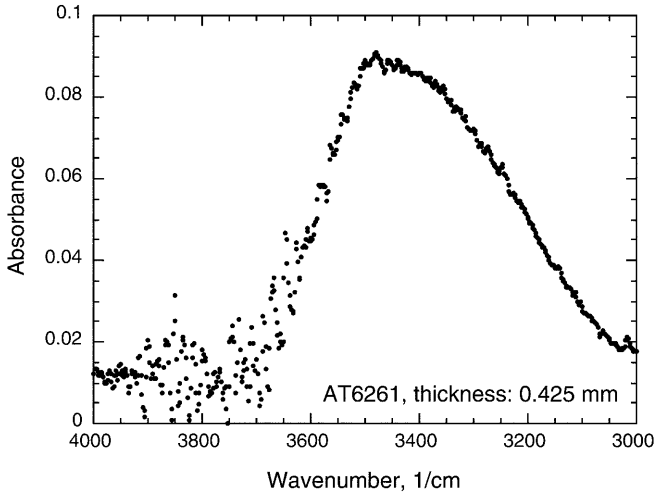

Fig. 1 Broad-band IR absorbance in specimen AT6261 attributed to the presence of molecular water

Elastic wave speed measurements

The ends of cylindrical specimens of approximately 10 mm diameter and 3 mm thickness were ground and polished optically flat and parallel to allow measurements of P and S wave speeds by ultrasonic interferometry. Because of the extreme sensitivity of elastic properties to the presence of porosity (particularly cracks), comparison of the wave speeds or moduli measured under bench-top conditions with the Hashin–Shtrikman averages calculated from single-crystal elastic constants provides a diagnostic measure of the crack density.

High-temperature mechanical testing

The apparatus which provides for torsional forced-oscillation and microcreep measurements at high temperature and pressure has been described in detail by Jackson and Paterson (1987, 1993). More recent improvements to the apparatus and specimen assembly have been reported by Jackson (2000). In particular, the installation of an internal furnace of improved design (by M.S. Paterson) has provided routine access to temperatures as high as 1300 °C, typically at 200 MPa confining pressure. The use of General Electric Lucalox grade polycrystalline alumina torsion rods, which behave almost elastically to 1300 °C, results in a substantially reduced background level of dissipation against which to resolve viscoelastic behaviour of the specimen itself. Use of tapered torsion rods and a suitably waisted thin-walled steel jacket allows the use of relatively small synthetic specimens (30 mm long and 12 mm in diameter).

In this study, the precision-ground synthetic olivine specimen was enclosed within high-purity Fe foil (99.95% purity, 50 μm thickness) in order to isolate it radially (two layers) from the mild steel jacket and longitudinally (single layer of foil) from the alumina torsion rods. Following annealing for 10–50 h at 1300 °C within the forced oscillation/microcreep apparatus, the specimen was cooled much more slowly (~1–3 °C min^{-1}) than in the experiments of Tan et al. (1997a), resulting in the virtual suppression of thermal microcracking.

Data processing

The conduct of both torsional forced oscillation and complementary torsional microcreep tests has been accorded greater emphasis than previously. A new and improved procedure for the quantitative analysis of the microcreep records (Jackson 2000) has been employed. The first stage is the fitting of an Andrade creep function of the form

$$J(t) = J_U + \beta t^n + t/\eta \qquad (1)$$

(e.g. Poirier 1985) to the time-dependent angular distortion per unit torque of the specimen assembly (inclusive of alumina and steel torsion rods and steel jacket). Here J_U is the instantaneous (unrelaxed) response, β is the coefficient of the transient term with exponent n typically fixed at 1/3, and $1/\eta$ is the "steady-state" creep rate. A corresponding creep record for the reference assembly, in which the specimen is replaced by a dummy specimen of Lucalox alumina, is similarly fitted to an Andrade model.[1] The complex torsional compliances for the two assemblies are then derived from the Laplace transforms of the respective creep functions. The parallel processing of the data for the specimen and reference assemblies then proceeds in the frequency domain exactly as for the forced oscillation data (Jackson and Paterson 1993).[2]

In the final step, the rheology manifest in the frequency-dependent shear modulus $G(\omega)$ and strain energy dissipation $Q^{-1}(\omega)$ inferred from the microcreep records, or more directly from the forced-oscillation experiments, is represented by either an Andrade model or a generalised Burgers model incorporating a specified distribution $D(\tau)$ of anelastic relaxation times τ (Jackson 2000; Appendix). The creep function for the Burgers model is

$$J(t) = J_U\{1 + \Delta \int_0^\infty D(\tau)[1 - \exp(-t/\tau)]\mathrm{d}\tau\} + t/\eta \ , \qquad (2)$$

with $D(\tau)$ given by

$$D(\tau) = \alpha\tau^{-(1-\alpha)}H(\tau - \tau_m)H(\tau_M - \tau)/(\tau_M^\alpha - \tau_m^\alpha) \ , \qquad (3)$$

where $H(x)$ is the Heaviside step function and $1 > \alpha > 0$. With this choice, Q^{-1} varies with frequency (or period T_o) approximately as $\omega^{-\alpha}$ (or T_o^α)within the absorption band (Minster and Anderson 1981) and linearly with T_o at much shorter and longer periods. Such absorption-band behaviour with $\alpha = 0.3 \pm 0.1$ is typical of the high-temperature internal friction "background".

These alternative Andrade and extended Burgers rheologies [with vector $\mathbf{a} = (J_U, \eta, \text{etc.})$ of model parameters] have been simultaneously fitted to the inferred frequency dependence of G and Q^{-1} through use of the iterative Levenberg–Marquardt strategy (Press et al. 1986) to minimise

$$\chi^2(\boldsymbol{a}) = \chi^2_G + \chi^2_{1/Q} = \sum_i \{[G_i - G(a;\omega_i)]^2/\sigma^2(G_i) + [Q_i^{-1} - Q^{-1}(\boldsymbol{a};\omega_i)]^2/\sigma^2(Q_i^{-1})\} \ . \qquad (4)$$

The functional forms of $G(\boldsymbol{a};\omega_i)$ and $Q^{-1}(\boldsymbol{a};\omega_i)$ appropriate for the Andrade and Burgers models are given in the Appendix. In the absence of well-determined a priori errors, the standard errors in G and Q^{-1} have been set at $\sigma(G)/G = 0.01$ and $\sigma(\log Q^{-1}) = 0.05$, the latter being equivalent to $\sigma(Q^{-1})/Q^{-1} = 0.12$.

[1] Gaps in the torsional microcreep dataset for the reference assembly have been filled by fitting the frequency dependence of its complex torsional compliance, as determined in forced oscillation tests, to the Andrade model, which is essentially the Laplace transform of Eq. (1).

[2] The torsional microcreep tests reported here were of total duration 5000 or 10 000 s. Each of these comprised five consecutive intervals during which the torque assumed values of 0, L, 0, −L and 0, respectively. These segments were either of equal duration or modified to allow relatively longer periods for observation of the extent to which the deformation is recoverable (anelastic) following removal of the applied torque. Processing of the 5000- and 10 000-s records in order to retrieve information for periods of 1–300 s and 1–1000 s, respectively, required a modest extrapolation from the domain 1–100 s of information concerning the viscoelasticity of the jacket material determined through forced oscillation tests on mild steel (Jackson et al. 2000).

Building upon the approximate power-law frequency dependence of Q^{-1} within the anelastic absorption band, one obtains a compact parameterisation of *both* the frequency and temperature dependence of Q^{-1} by requiring that $Q^{-1} = Q^{-1}(\omega\tau)$ where $1/\tau$ is a representative thermally activated relaxation rate with activation energy E:

$$Q^{-1}(T_o, T) = AT_o^{\alpha} \exp(-\alpha E/RT) \ . \quad (5)$$

Use of Eq. (5) is appropriate only where the distribution $D(\tau)$ of relaxation times, or equivalently the power-law exponent α, is essentially independent of temperature (Jackson et al. 2000).

Provided that $Q^{-1} \ll 1$, the modulus dispersion associated with the power-law dependence of $Q^{-1} \sim T_o^{\alpha}$ in the neighbourhood of a suitable reference period T_o^{ref} is given by

$$G(T_o)/G(T_o^{ref}) = 1 - \tan[\pi(1-\alpha)/2][Q^{-1}(T_o) - Q^{-1}(T_o^{ref})] \quad (6)$$

(Brennan and Smylie 1981). This low-loss approximation has previously been employed in reporting results from this laboratory (Webb et al. 1999; Jackson et al. 2000) and is retained here for the description of the viscoelastic behaviour of the iron foil liner and jacket material. However, there are two disadvantages to this parameterisation. Firstly, the power law (with the logarithmic derivative $\gamma = \partial \ln Q^{-1}/\partial \ln T_o = \alpha$, a constant) often systematically misfits the forced oscillation $Q^{-1}(T_o)$ data, which typically suggest that γ increases mildly with increasing period. Secondly, and more importantly, the approximate expression (Eq. 6) for the dispersion breaks down when the low-loss condition $Q^{-1} \ll 1$ is no longer satisfied, substantially overestimating the dispersion, especially at very long periods.

For these reasons it makes sense to discontinue the practice of reporting experimental results in terms of the low-loss approximation to the dispersion associated with power-law dissipation, favouring instead the use of either the Andrade or extended Burgers models. Each of these has a functional form that requires γ to increase with increasing period, from n to 1-n for the Andrade model, and to vary from α 1 at short periods through α well within the absorption band to 1 at long periods for the Burgers model. Moreover, the internal consistency inherent in this approach means that the Kramers–Kronig relationship linking dissipation and dispersion is automatically satisfied.

Microstructural characterisation of the polycrystalline olivine aggregates

Generalities

Details of the preparation of specimens, along with measured densities, average grain sizes, bench-top ultrasonic wavespeeds and [H_2O] contents are presented in Table 1 not only for hot-pressed (HP) but also for the same specimens (AT) after mechanical testing.

Measured densities indicate a close approach (within 2% – Table 1) to the theoretical density expected for natural Fo_{90} olivine (3.338 g cm^{-3}, Brown 1980). The anisotropy of thermal expansivity of single-crystal olivine results in the development of substantial intergranular stresses during the heating and cooling of polycrystalline material. Under unfavourable circumstances, as in coarse-grained ultramafic rocks, these stresses can cause microcracking. The combination of relatively small grain size, long periods of annealing at high temperature and slow subsequent cooling has minimised, but not completely eliminated, the impact of thermal microcracking in the specimens examined in this study. Both inter- and transgranular cracking can definitely be recognised in the thin sections, in general agreement with inferences made from measurements of mechanical properties. Of course, the direct observations of cracks should be interpreted with caution since thin specimen preparation could have produced some of this cracking.

Low pore volumes estimated from the microstructural studies are broadly consistent with the high densities measured for these aggregates. Pores inside grains are always smooth and approach spherical shape whereas pores in grain boundaries are much more angular and characteristically have higher aspect ratios (maximum/minimum dimension).

Copper, as rounded particles of dimension ca. 1–2 μm, is the major impurity (≤0.5 vol%) throughout these aggregates, probably attributable to contamination from the brass sieve during preparation of olivine powder. In general, the Cu impurity is more abundant in samples prepared from finer-grained powders. In the set of samples discussed here, specimens labelled 6328 with 2–10 μm starting grain size have the most Cu impurity at ca. 0.5%. The metal composition can be explained if the Zn from the brass were oxidised and incorporated as a dilute solution (~0.1 mol%) of Zn_2SiO_4 in olivine during heat treatment. The Cu-rich metal bodies are presumably molten above ~1000 °C and do not appear to impede grain boundary motion since the majority of blebs are found as inclusions inside grains. Blebs are, however, also common at grain boundaries and grain junctions. Very close to specimen surfaces, Fe–Ni metal blebs become dominant – see below for the explanation.

By combining the observations from light and electron microscopy, we are confident that silicate melt volumes are well below 0.1 vol% in all specimens, most likely even below 0.01%, but this is very difficult to measure. The melts are concentrated at grain boundaries, particularly in grain-edge triple junctions (Fig. 2b), where the melt structures are as small as a few nanometres across. Larger, optically visible melt bodies are quite rare. There is also some association between melts and pores – especially at grain boundaries where the angular pore terminations commonly feature minor volumes of melt.

Given our experience reported previously in Tan et al. (1997a), particular attention has been paid to the microstructures in the vicinity of the interfaces between the olivine and the Fe foils used at either end of the specimen and between its cylindrical surface and the mild steel jacket. At the ends of specimen AT6261, the intimate contact against the Fe foil separating the alumina torsion rod from the olivine specimen was carefully searched, using SEM for evidence of reaction. No silicate/oxide other than olivine was found. Widely dispersed metal blebs (mainly less than 5 μm in diameter) were observed within olivine in the neighbourhood of the interface (~50 μm). The metal blebs are actually Ni–Fe alloys with an Ni/Fe ratio that increases systematically with increasing distance from the interface. The olivine adjacent to the interface is enriched in iron

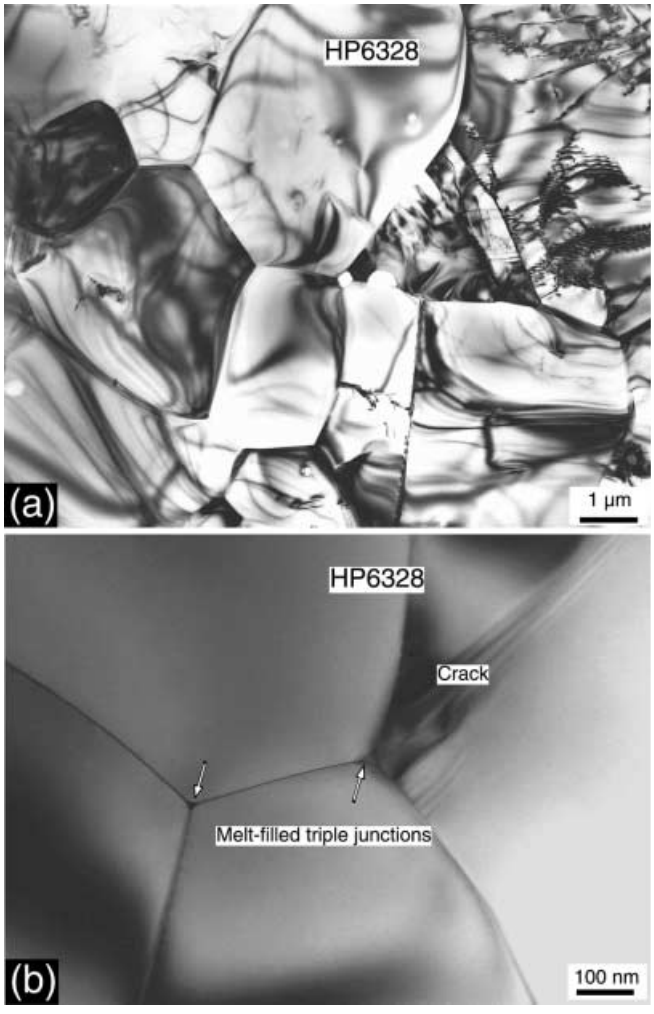

Fig. 2 **a** TEM bright-field image highlighting the generally low but variable dislocation density for specimen HP6328, but typical also of other specimens in this suite. **b** TEM bright-field image showing grain-boundary morphology and small melt-filled grain-edge tubules (*arrowed*) in specimen HP6328

(FeO ~16 wt%) without departing measurably from (Mg + Fe)/Si stoichiometry. These observations are reminiscent of those of Raterron et al. (1998), which were plausibly interpreted in terms of reactions between metallic iron and point defects formed during the prior exposure of San Carlos olivine to relatively oxidising conditions in nature. These defects are principally ferric iron ($Fe^{\bullet}_{oct}$) and vacancies (V''_{oct}) on the octahedral sites and ferric iron (Fe'_{tet}) or vacancies (V''_{tet}) on the tetrahedral sites in concentrations reaching about 1000 ppm within the fayalite stability field (Nakamura and Schmalzried 1983). Such mildly oxygen-enriched olivine containing both ferric iron and cation vacancies can be reduced homogeneously (i.e. without the precipitation of an additional phase) by metallic iron through the defect reaction

$$Fe(m) + V''_{oct} + 2Fe^{\bullet}_{oct} = 3Fe^{\times}_{oct} \quad (7)$$

(Raterron et al. 1998).

Conditions were evidently somewhat different at the interface between the cylindrical surface of the olivine specimen and the Fe foil lining the steel jacket. Here, there is evidence of a thin layer (~3 μm) of orthopyroxene, presumably reflecting the reduction mainly of the minor Ni_2SiO_4 component of the olivine according to the reaction:

$$Mg_2SiO_4\ (ol) + M_2SiO_4\ (ol) \rightarrow Mg_2Si_2O_6\ (opx) + 2M\ (metal) + O_2 \quad (8)$$

with M = Ni, Fe. In these cylindrical surface regions, the Ni–Fe blebs extend as far as 150 μm into the olivine aggregate with most of these being at or near olivine grain boundaries. The abundance of Ni–Fe blebs increases towards the specimen surface. At the very edge of the specimens, the Fe foil has commonly been injected in bulk up to 10 μm along many of the silicate grain boundaries.

Some grain boundaries (GBs) deep inside the specimen were cracked open or contained obvious melt or impurity structures and were not further examined by TEM. Selected "simple" GBs were carefully examined using methods described by Drury and Fitz Gerald (1996). One characteristic of GBs from the suite of samples in Table 1 that is common to those reported by Drury and Fitz Gerald is the minimum image width: despite extremely careful tilting and focusing in TEM, the width of any GB image could not be made smaller than 1 nm. Interpreting GB images at such high resolution is difficult [see e.g. Vaughan et al. (1982), Jin et al. (1998) or de Kloe et al. (2000) for more details of GB imaging] so X-ray analyses were used to check for the existence of GB films or impurity segregations. These X-ray measurements had to be performed painstakingly to minimise element loss during analysis and one approach in olivine-olivine GBs is to involve broad-beam analysis to check for elements such as Ca and Al. Rather than attempt to estimate a composition for a GB structure whose thickness and chemical variation are unknown but much smaller than the analytical probe, we followed Drury and Fitz Gerald (1996) and measured here only peak-to-background ratios, essentially to indicate whether impurity was present or not, with reference measurements made nearby in the grain interiors used to indicate local background concentration levels.

Figure 3a shows three GBs and a junction in AT6261 which were imaged (all 1 nm or wider images) and analysed using X-rays. Also shown schematically in Fig. 3a are two analysis positions, one at a GB, one in the adjacent grain, to represent the "large" analytical probe and to contrast between GB analysis and non-GB analysis. The best results were always obtained from GBs that were aligned in the TEM tilting stage to be parallel to the incident electron beam, and with the TEM probe elongated parallel to the GB trace. Probe dimensions were about 25 × 250 nm (full width, one-tenth maximum). Typical results for Ca peak/background versus Al peak/background are plotted in Fig. 3b. For all aggregates examined here, both Ca and Al peak/

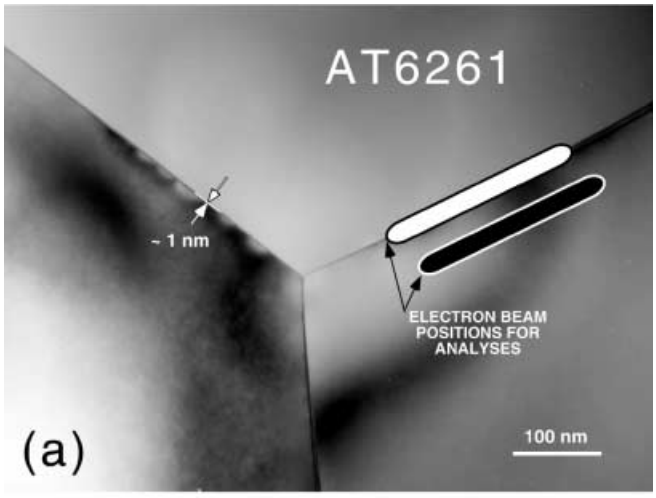

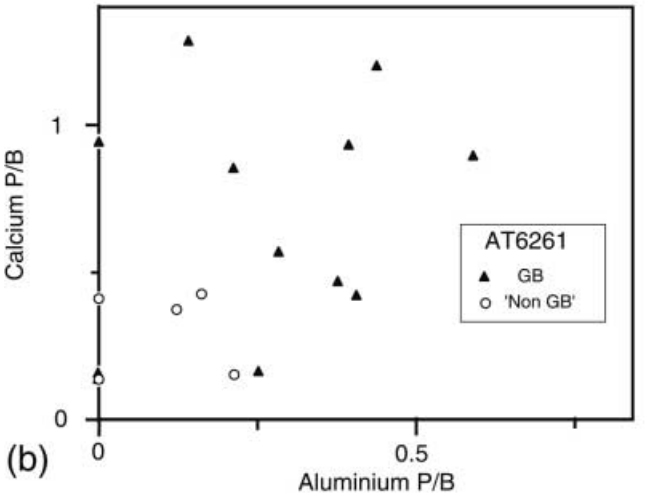

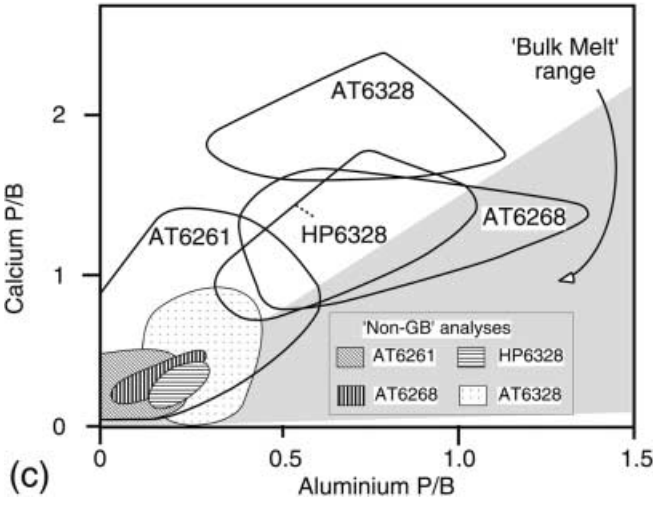

Fig. 3 a Bright-field TEM micrograph of one grain junction in AT6261 with the junction axis tilted to be parallel to the electron beam. If melt is present at this junction, its cross-sectional dimension must be below ca. 2 nm. The three GBs here showed narrowest image widths of ca. 1 nm (note that most parts of the GBs in this image are not exactly parallel to the incident beam so they appear wider than this 1 nm minimum). Electron probe positions for GB analysis are shown schematically both for a GB and a non-GB analysis. **b** X-ray intensities for Ca and Al in AT6261 measured for both GBs and adjacent grains. The Ca and Al signals are so weak that it makes no sense to quote chemical composition (peak/background values are usually less than 1) so the raw peak/background (*P*/*B*) results are plotted instead. The analytical uncertainty in the P/B values ranges typically from 20–40% of the value for the *GB* analyses to 100% or greater for the *Non-GB* results. **c** Ca and Al intensity measurements for the whole sample suite, again plotted as peak/background. Results are summarised as fields of values grouped by specimen. Fields for non-GB analyses are shown *patterned*, fields for GB analyses are *open with thick border* and *individually labelled*. A comparative field based on bulk melt analyses (note that bulk melts, producing high *P*/*B* for Ca and Al peaks, plot *far to the right* of the figure) is represented by the *greyed wedge* and labelled *Bulk Melt* range. Numbers of analyses represented by fields for, respectively, GB and non-GB analyses, were AT6261: 12 and 5, AT6268: 7 and 4, HP6328: 8 and 4 and AT6328: 7 and 7

background values (represented as fields in Fig. 3c for different specimens) are higher for GB analyses, indicating enhancement of both elements in the GB region. Given the continuous 1-nm-wide images recorded for the corresponding GBs, some might wish to infer the existence of continuous thin melt films along all olivine-olivine GBs in our materials, but in reality using this broad beam analytical approach, we cannot dismiss the alternative possibility of nanometre-scale chemical profiles or segregations in and adjacent to the GBs. However, one firm conclusion can be reached – away from detectable melt structures the simple GB regions, whatever their nanostructures, are enriched in elements that are incompatible impurities in the adjacent olivine.

To give some indication of how these peak/background values could relate to chemical composition, the ratio Ca peak/background versus Al peak/background was also measured for 16 melt bodies in these specimens. Values range widely from 1.3 to 0.1 (grey wedge plotted in Fig. 3c) and average 0.34 ± 0.34. Note that the GB fields for all samples appear to plot near or beyond the Ca-rich side of that bulk melt range. Is this a robust feature of the GB chemistry or are analyses biased by the large uncertainty in determining the peak/background ratio of a tiny Al peak situated in the X-ray spectrum between large Mg and Si peaks arising from surrounding olivine? (In contrast, peak/background of the correspondingly tiny Ca peak can be determined with more confidence because its energy is far from any olivine-related peaks). That the Al peak/background is consistently smaller for the non-GB analyses suggests that the difference between GB and melt chemistries is truly robust. A similar conclusion of Ca enrichment of olivine GB regions was recently published by de Kloe et al. (2000), who used more sophisticated analytical TEM methods and much smaller incident probes.

Specimen 6261

Specimen HP6261 is texturally well equilibrated and of relatively uniform grain size averaging 25 μm. A few thermal cracks, mainly along grain boundaries, were

seen. Pores of <1–5 μm diameter are widely distributed throughout the grains and in grain boundaries. Some larger grains contain over 100 pores visible in the light microscope. A thin section decorated by oxidation reveals a dislocation density that varies significantly from grain to grain. Some larger grains show subgrain boundaries. The lattice rotation associated with these dislocations is only minor – undulatory extinction is almost undetected in the polarised light microscope.

This material was subsequently exposed to the maximum temperature of 1300 °C for a total of 63 h during mechanical testing. The final microstructure of AT6261 (Fig. 4a) is very similar to that for the hot-pressed specimen. Grain growth was limited with average grain size increasing modestly only to 30 μm. In our initial examination of the petrographic thin section, very few thermal cracks were seen. However reexamination of the same thin section several weeks after it was prepared revealed that cracks had developed on about one third of grain boundaries, presumably in response to residual intergranular stresses of thermal origin. The occurrence of thermal microcracking following recovery of the specimen from the high-pressure environment in which the mechanical testing was performed is corroborated by the relatively low wavespeeds measured on this specimen some months later (Table 1). Evidence of chains of tiny pores inside grains and GBs points to crack-healing during the high-temperature history of the specimen. Some of the recovered grain boundaries are cracked open with apertures of several to tens of nanometres as seen in TEM.

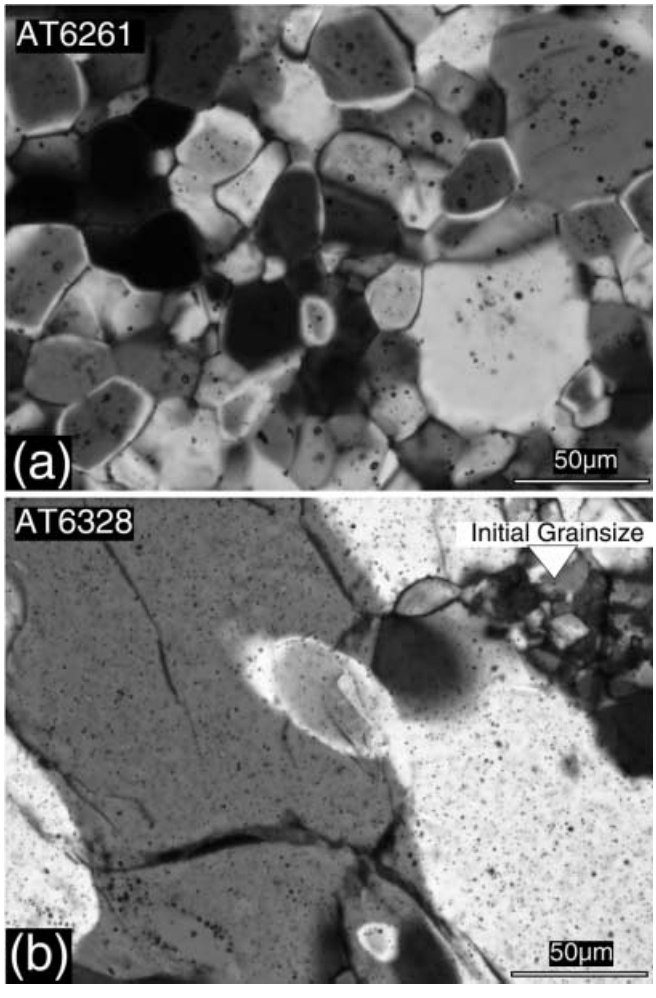

Fig. 4a, b Transmitted light micrographs of specimens AT6261 **a** and AT6328 **b**. In the AT6328 region shown, the relict patch of fine-grained material is representative of the microstructure (of HP6328) prior to abnormal grain growth during mechanical testing

Comparison of the infrared absorption measured on the HP and AT specimens reveals substantial but incomplete dehydration during the mechanical testing at high temperature and pressure (Table 1). This observation stands in marked contrast with the experience with the similarly prepared specimen 6265 (Tan et al. 1997a) where all of the 100 ppm H_2O present in the hot-pressed specimen was lost from the specimen during subsequent mechanical testing.

The Cu-metal content is around 0.1 vol% and the silicate melt volume clearly below 0.1 vol% for both HP and AT materials. Only tiny melt volumes are found at pores and grain boundaries of AT6261 and many triple junctions are apparently melt-free at a resolution of 2 nm (Fig. 3a). Those melt structures present are most likely totally unconnected. The GB X-ray analyses (Fig. 3) point to segregations of Ca and Al on all simple GBs away from melt regions.

Tiny flakes of graphite were identified in some pores and GBs of AT6261 using TEM. These comprise a very minor contaminant and can be attributed to the combination of residues from organic liquids used during grinding and grain-size sorting by sedimentation of San Carlos powders, together with the low drying temperature (only 150 °C) for specimen 6261.

Specimen 6268

Relatively high density (~98%) was achieved by hot-pressing prefired powder of 10–38 μm grain size at 1300 °C for an extended period of 14 h in two separate runs, nos. 6268 and 6269. Water/hydroxyl was almost undetectable in the hot-pressed specimen (Table 1) whose microstructure shows a markedly bimodal distribution of grain size which averages 15 μm. The large grains, typically a few tens of micrometres in diameter, have been weakly deformed, showing ubiquitous undulatory extinction, deformation bands and blocky subgrains, and are typically rimmed by small undeformed grains (<10 μm in diameter), presumably the result of recrystallisation of grain exteriors crushed during cold-pressing. An ideal texture has not been achieved, despite the annealing at 1300 °C. The mechanically tested specimen (Fig. 5) showed a grain size and microstructure indistinguishable from the above, despite being held for a further 10 h at 1300 °C during mechanical testing. While the grain structure might look complex at low magnification (Fig. 5a), the boundaries of the small grains seen in TEM are smooth and regular (Fig. 5b). The disloca-

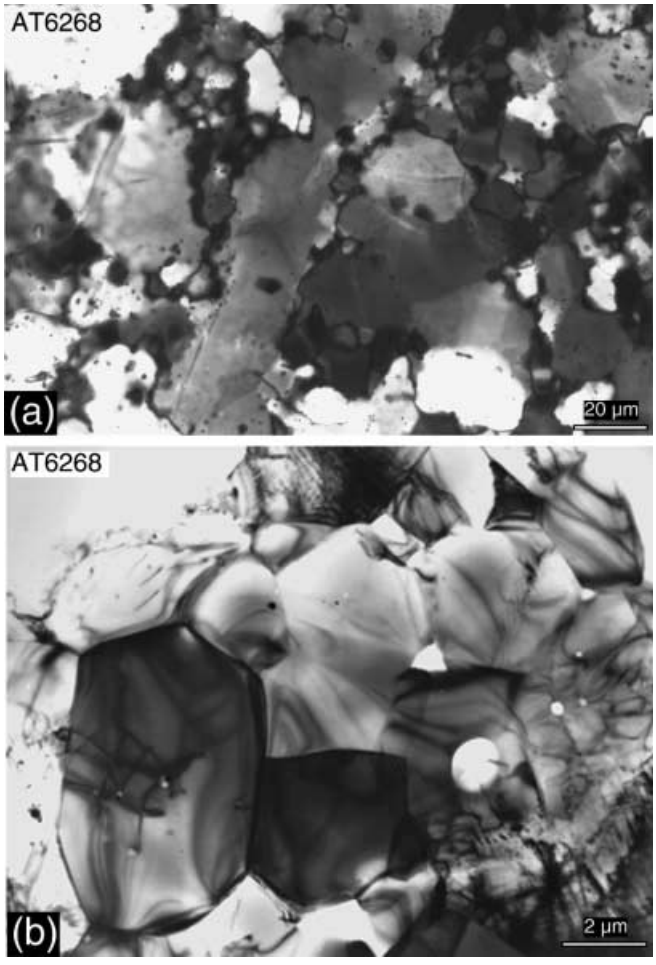

Fig. 5 **a** Transmitted light micrograph of specimen AT6268 showing highly deformed larger grains a few tens of micrometres in diameter rimmed by mantles composed of smaller (< 10 μm) undeformed grains. **b** TEM bright-field micrograph of the fine-grained mantle material revealing relatively well-equilibrated texture along with some residual porosity

tion density is higher in the (relict) larger grains than in the small (recrystallised) rim grains. The virtual absence of water in the prefired precursor powder is probably responsible for the sluggish textural evolution during hot-pressing and subsequent mechanical testing.

Pores are present in this specimen but occur dominantly in GBs and are therefore concentrated in the finer-grained rims. Larger pores (up to 5 μm) have taken on very irregular and angular shapes. While some cracks occur in the AT thin section, this is the least cracked of the three materials. The Cu-rich metal content inside this specimen is around 0.1%, and the melt content is well below 0.1%. GBs away from melt regions again show definite Ca and Al enrichment (Fig. 3c).

Specimen 6328

The microstructure of the hot-pressed specimen comprises fine grains with fairly uniform grain-size distribution. The grains are estimated to have about 8 μm average diameter, and GBs are smooth and regular. TEM reveals that dislocation density is variable (Fig. 2a) with some smaller dislocation-free grains presumably having grown at the expense of larger deformed grains. Tiny pores (< 1 μm) occur throughout. The light microscope reveals small numbers of isolated, distinctly larger grains 25 to 100 μm across. The only cracks are seen around these coarser grains and high elastic wave speeds were proven in subsequent bench-top ultrasonic measurements (Table 1). A few macroscopic cracks ~2 mm in length are observed at the ends of the specimen, presumably resulting from stresses caused by the large contrast in the thermal expansivity between the olivine and the alumina. The cracked ends of the hot-pressed product were removed during preparation of the specimen for mechanical testing. The Cu-rich metal content inside this material (prepared from the powder of smaller particle size – Table 1) is about 0.5%. Melt could not be identified with the light microscope although some grain triple junctions with tiny melt structures are visible in TEM (Fig. 2b). The melt content is estimated again to be well below 0.1%.

Following the mechanical testing, special care was taken to characterise the microstructure of the AT specimen, in order to explain the dramatic evolution in the mechanical behaviour observed at 1300 °C (see below). Two transverse thin sections were cut near the ends, as well as a central longitudinal section of the entire specimen. Near the ends, a significant portion of grains had undergone abnormal grain growth to form grains which are elongated parallel to (0 1 0) with lengths reaching 200 μm, within a matrix of residual fine-grained (< 10 μm) material. These regions of highly bimodal grain-size distribution give way within 2 mm from the ends of the specimen and from its cylindrical surface to a more uniform grain size averaging ~150 μm in the central part of the specimen (Fig. 4b). The grain shapes while elongated are quite complex and presumably involve local migration after the rapid abnormal growth was exhausted. The big grains are undeformed as seen from both the lack of undulatory extinction and the low dislocation densities. This coarse-grained specimen is pervasively microcracked, and essentially melt-free at light microscope scale. A few healed cracks (marked by dislocations and metal blebs) indicate some crack healing. The ca. 0.5% of Cu-rich metal occurs in < 1 to 2 μm blebs distributed uniformly throughout grains and GBs. Tiny pores (ca 1 μm) are present throughout, sometimes attached to a metal bleb. Larger pores (to 2 μm) appear to define central seed regions around 25 μm in diameter within some of the big grains. Melts are common along GBs of the big grains in the form of three-dimensional lenses, some of them including one Cu-rich metal sphere, and elongate along the GB; these lenses can be 0.3 μm at their thickest and extend up to 2 μm along the GB. From the TEM thin foil, it was estimated that 2% of the GB is decorated by such melt lenses – this corresponds for the 150 μm grain size to a melt fraction of only

<0.01 vol%. Presumably the abnormally mobile GBs swept up melts (but not metals to any great extent) which originally were dispersed in tiny structures throughout the fine-grained hot-pressed precursor. A small patch of fine-grained material preserved deep inside the generally coarse-grained AT specimen is shown in Fig. 4b, where it occupies one of the interstices between larger grains.

For specimen 6328, GB analyses were conducted in HP and AT states. In both cases, GBs away from melt regions are systematically enriched in Ca and Al relative to grain interiors. There is also a change in the chemical signature associated with the marked grain growth: GBs in AT6328 are somewhat richer in Ca (Fig. 3c). It could be speculated that the extra GB enrichment in AT6328 reflects the abnormally fast GB migration.

Results of mechanical testing: torsional forced oscillation and microcreep

Specimen 6261

Testing protocol

Testing of the experimental assembly containing specimen 6261 involved four successive excursions between room temperature and 1300 °C under a confining pressure of 200 MPa. Here we emphasise the results of the torsional forced oscillation and microcreep tests performed during the prolonged fourth and final thermal cycle. These are preferred to earlier measurements on the grounds of more thorough high-temperature annealing, better alignment of the capacitance displacement transducers and the slower staged cooling of the final cycle. Mechanical tests were repeated at intervals during a long period (47 h) of annealing at 1300 °C, and during subsequent slow, staged cooling ($\sim$1 °C min^{-1}) to room temperature. At most temperatures, especially for $T \geq 1000$ °C, at least 1 h was allowed prior to the conduct of the forced-oscillation/microcreep tests for approach to thermal and mechanical equilibrium.

Torsional microcreep tests

The time-dependent deformation of the specimen assembly recorded in microcreep test 890-5 conducted on specimen 6261 at 1300 °C is shown in Fig. 6a. The instantaneous (elastic) and time-dependent (anelastic and viscous) contributions are readily identified and the misfit relative to the optimal Andrade ($n = 1/3$) model (Jackson 2000) is presented. More definitive examination of the extent to which the non-elastic deformation is recoverable (i.e. truly anelastic) is provided by alternative testing protocols in which more time is allowed for observation of the recovery than for torque application. Because the deformation of the Lucalox alumina/steel reference assembly departs only negligibly from the elastic ideal even at 1300 °C (Jackson 2000 Fig. 2c), the creep observed in records such as those of Fig. 6 is overwhelmingly attributable to the specimen itself. Notably, much smaller amounts of non-elastic strain have been measured at lower temperature (Fig. 6b). The total non-elastic distortion accumulated during 2000 s of exposure to the applied torque has diminished to less than 50% of the elastic strain at 1200 °C, and is barely visible at 1000 °C.

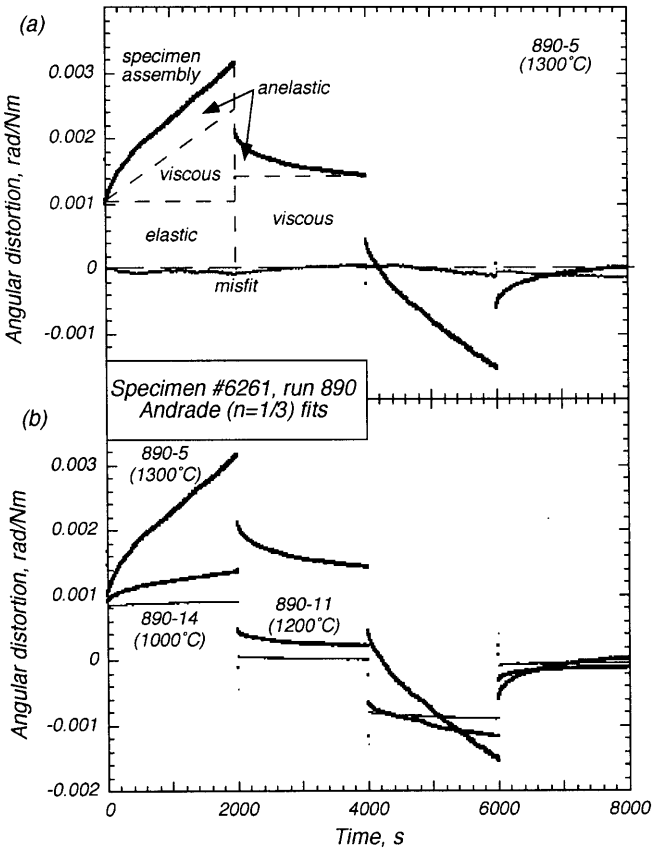

Fig. 6a, b Torsional microcreep records obtained during the final run no. 890 on specimen 6261. The second and fourth segments of each record, during which the applied torque was zero, allow assessment of the recoverability of the creep strain accumulated during periods of positive (first segment) and negative (third segment) torque application. **a** Angular distortion of the specimen assembly for test 890-5 (1300 °C, Table 2) along with the misfit relative to the best-fitting Andrade model. The elastic, anelastic (time-dependent recoverable), and viscous (time-dependent irrecoverable) components of the total deformation are *labelled*. **b** Comparison of microcreep records 890-5, -11 and -14 showing the temperature sensitivity of the creep response

Alternative Andrade and extended Burgers rheologies

Alternative Andrade and extended Burgers rheologies fitted to the modulus dispersion and dissipation inferred from the forced oscillation and microcreep tests during this final thermal cycle are presented in Table 2. For the Andrade model, it is possible simultaneously to refine all four of the model parameters (J_U, n, β, η) in fitting the

Table 2 Andrade and extended Burgers rheologies fitted to torsional forced-oscillation[a] and microcreep[b] data for specimen 6261 tested in run 890 during a total of 47 h continuous exposure to conditions of 1300 °C and 200 MPa, and during subsequent staged cooling to room temperature. For details of the calculation of $G(T_o)$ and $Q^{-1}(T_o)$ from model parameters see the Appendix

Run no. Prior anneal[c] >h<	Fit[d]	$\chi^{2(e)}$	$J_U/10^{-1}$ GPa^{-1}	Δ or $\beta/10^{-2}$ β: GPa^{-1} s^{-n}	α or n	log[τ_m (s)]	log[τ_M (s)]	$\eta/10^4$ GPa s
Temperature: 1300 °C								
890-1(O) 2.5	A-FePL[f]	0.54	0.204(39)	0.93(37)	0.18(10)			0.21(14)
890-2(CS) 3.0	A-FePL	2.08	0.226(6)	0.94(6)	0.32(2)			1.28(38)
	B-FePL	1.30	0.243(4)	2.26(23)	0.32(2)	(−2)	2.83(22)	0.85(12)
890-3(CV) 6.5	A-FePL	1.71	0.226(5)	0.78(6)	0.31(2)			1.53(45)
	B-FePL	1.20	0.240(3)	1.96(21)	0.32(2)	(−2)	2.90(24)	1.07(17)
890-4(O) 9.5	A-FePL[g]	3.19	0.191(37)	0.98(37)	0.16(7)			0.33(17)
890-5(CS) 21.5	A-FePL	1.26	0.224(4)	0.55(4)	0.31(2)			1.44(32)
	B-FePL	0.72	0.234(3)	1.48(27)	0.31(3)	(−2)	2.97(38)	1.13(23)
890-6(CV) 25.0	A-FePL	1.42	0.223(5)	0.65(5)	0.31(2)			1.91(60)
	B-FePL	0.13	0.236(3)	1.21(23)	0.32(2)	(−2)	2.48(27)	1.03(25)
890-7(O) 29.0	A-FePL	3.41	0.192(18)	0.78(19)	0.17(4)			0.56(14)
890-8(O) 30.5	A-FePL	1.85	0.187(22)	0.86(22)	0.16(4)			0.59(15)
	A-FePL	6.91	0.208(9)	0.64(9)	0.22(3)			(1.5)[h]
890-9(O) 45.2	A-FePL	10.44	0.196(11)	0.59(11)	0.22(4)			0.85(32)
Temperature: 1200 °C								
890-10(O)	A-FePL	3.37	0.171(8)	0.40(9)	0.19(5)			2.63(177)
890-11(CS)	A-FePL	0.14	0.187(2)	0.215(18)	0.33(2)			6.28(258)
	B-FePL	0.03	0.191(1)	0.71(45)	0.34(3)	(−2)	2.79(88)	3.82(200)
Temperature: 1100 °C								
890-12(O)	A-FePL	9.43	0.162(4)	0.19(5)	0.20(6)			8.37(1025)
Temperature: 1000 °C								
890-13(O)	A-FePL	5.93	0.154(5)	0.099(46)	0.124(67)			8.41(401)
	A-FePL	6.71	0.148(8)	0.152(76)	0.074(39)			(6)[h]
890-14(CS)	A-FePL	0.70	0.166(1)	0.021(2)	0.43(4)			6.12(116)
	B-FePL	0.66	0.166(1)	0.190(33)	0.43(19)	(−2)	3.21(163)	5.59(74)
Temperature: 900 °C								
890-15(O)	FeM	$\langle G\rangle^{i} = 69.70(66)$		$\langle Q^{-1}\rangle^{i} = 0.0082(14)$				
Temperature: 800 °C								
890-16(O)	FeM	$\langle G\rangle^{i} = 64.19(69)$		$\langle Q^{-1}\rangle^{i} = 0.0077(13)$				
Temperature: 600 °C								
890-17(O)	FeM	$\langle G\rangle^{i} = 70.58(43)$		$\langle Q^{-1}\rangle^{i} = 0.0035(11)$				
Temperature: 400 °C								
890-18(O)	FeM	$\langle G\rangle^{i} = 73.88(63)$		$\langle Q^{-1}\rangle^{i} = 0.0015(15)$				
Temperature: 200 °C								
890-19(O)	FeM	$\langle G\rangle^{i} = 76.26(44)$		$\langle Q^{-1}\rangle^{i} = 0.0003(16)$				
Temperature: 20 °C								
890-21(O)	FeM	$\langle G\rangle^{i} = 82.16(48)$		$\langle Q^{-1}\rangle^{i} = 0.0010(12)$				

[a] Forced-oscillation data 'O' for periods of 1–100 s unless otherwise indicated

[b] Microcreep records of 10 000 s total duration. The labels 'CS' and 'CV' refer to different combinations of torque application and recovery intervals (given in seconds by (2000, 2000) and (1000, 3000), respectively – see text for detailed description of testing protocol. Both types of microcreep record were processed to retrieve information concerning the response for periods of 1–1020 s

[c] Prior exposure to 1300 °C, 200 MPa during present run; additional 15.5 h exposure during preliminary runs 888 and 889; forced oscillation data (888-4, 5 and 7 and 889-1) and microcreep data (888-6) reveal systematically lower values of modulus and higher dissipation – in accord with the temporal evolution of these properties observed at 1300 °C during run 890

[d] Labels '*A-FePL*' and '*B-FePL*' indicate use of Andrade and extended Burgers models, respectively, for description of the viscoelastic behaviour of the unknown, along with a parameterisation of the viscoelasticity of the mild steel jacket and Fe liner based on $Q^{-1} \sim T_0{}^{\alpha}$ and associated modulus dispersion (Eq. 6). The label '*FeM*' denotes a more cumbersome strategy for the modelling of the mild steel jacket/iron liner in which the shear modulus and dissipation for mild steel were incorporated pointwise into the analysis. Outer diameter of the jacketed specimen: 12.62 mm

[e] Errors used in calculation of χ^2: $\sigma(G)/G = 0.01$, $\sigma(\log Q^{-1}) = 0.05$

[f] 1–15-s oscillation period

[g] 1–28-s oscillation period

[h] Regression performed with η fixed at value suggested by analysis of microcreep records

[i] Average values of G and Q^{-1} only for $T = 900$ °C where dissipation and dispersion are both small

viscoelastic behaviour for temperatures ≥ 1000 °C. With the six-parameter extended Burgers rheology, it is usually not possible to refine the value of τ_m. Instead a five-parameter (J_U, Δ, α, τ_M, η) refinement is undertaken with τ_m fixed at 0.01 s.

Strong covariance among model parameters is characteristic of both the Andrade and Burgers models. For the Andrade rheology, the fact that $\partial J/\partial t = n\beta t^{n-1} + 1/\eta$ $(0 < n < 1)$ becomes infinite at $t = 0$ makes the instantaneous response given by J_U difficult to separate from the short-term anelastic behaviour. This is expressed in strong covariance among J_U, β and n. Similarly, for the Burgers model, greater width ascribed to the anelastic absorption band (τ_m, τ_M) carries the corollary of larger anelastic relaxation strength Δ and correspondingly diminished viscous relaxation requiring increased viscosity η.

These alternative rheological models typically fit the data pertaining to the period range 1–100 s (forced oscillation) and 1–1000 s (microcreep) equally well (e.g. Fig. 7), provided that a sufficiently wide anelastic absorption band is allowed for the Burgers model. The observations require $\tau_m \leq 0.01$ s and $100 \leq \tau_M \leq 1000$ s, the value of τ_M being tightly constrained by the non-linear regression at 1300 °C but less so at lower temperatures (Table 2). Despite the similarity between their descriptions of the absorption band, the Andrade and Burgers models show markedly different asymptotic behaviour at both short and long periods, most clearly evident in the period or frequency dependence of Q^{-1} (Fig. 7b; see also Experimental Methods: Data Processing above). The viscosity associated with the Burgers model is consistently lower than that for the corresponding Andrade model (Table 2) – reflecting the fact that all relaxation at periods substantially longer than τ_M must be attributed to viscous behaviour, whereas for the Andrade model the distribution of anelastic relaxation times is infinitely wide (Jackson 2000).

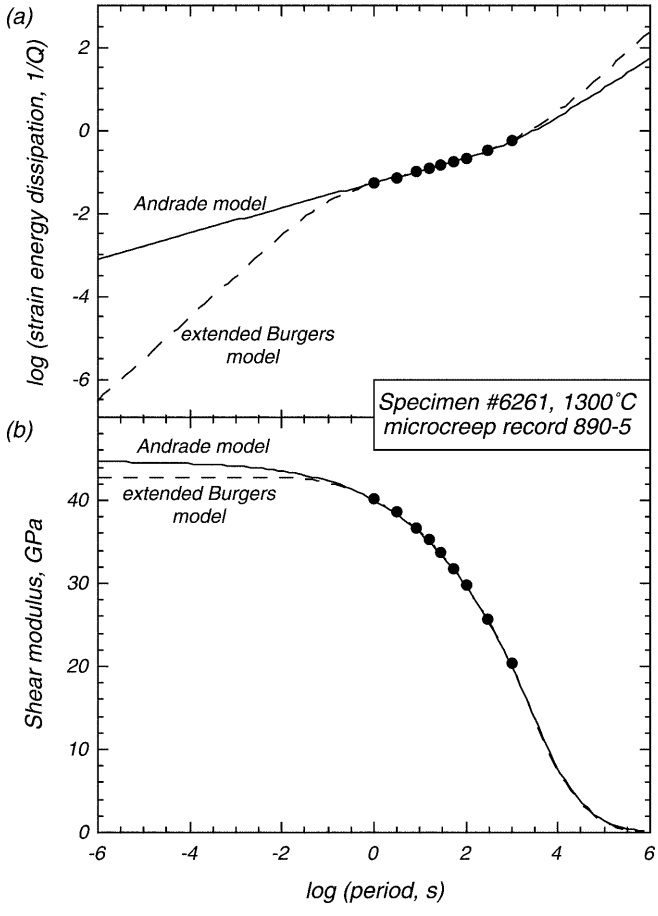

Fig. 7a, b Andrade and extended Burgers model fits (Table 2) to **a** the modulus dispersion and **b** the dissipation information extracted from microcreep record 890-5 at 1300 °C. The alternative rheologies fit the data (indicated by the *plotting symbol*) equally well but diverge substantially in the description of Q^{-1} at much shorter and longer periods

Comparison of forced-oscillation and microcreep data

The dispersion and dissipation inferred from the forced-oscillation and microcreep data are broadly consistent (e.g. Fig. 8), as are the fitted rheologies (Table 2), though not without significant differences of detail. The inferences concerning mechanical behaviour from the forced-oscillation data, being obtained relatively directly, are considered to be the more quantitatively robust. Also, comparisons, for example, between the results of the temporally closely spaced forced-oscillation tests 890-7 and 890-8 reveal a high degree of reproducibility (Fig. 8). The processing of the microcreep records involves a hierarchy of assumptions and/or approximations. Two of these are likely to affect adversely the reliability of the behaviour inferred from the microcreep records at short periods. These are the use of the Andrade model with the exponent n fixed at 1/3 in the time-domain fitting of the raw microcreep records for the specimen assembly (Fig. 6), and the absence of a procedure to allow correction of the microcreep records for the influence of the interaction with the dense gas-pressure medium–known from forced-oscillation measurements to require a correction that is significant for periods less than 10 s (Jackson and Paterson 1987). Nevertheless, the microcreep records provide vital information concerning the extent to which the non-elastic deformation is recoverable, and, given their sampling of longer period behaviour, have the potential to provide tighter constraints on the viscosity.

Temporal evolution of the mechanical behaviour

Consistent temporal evolution towards higher modulus and lower dissipation is evident amongst the forced-oscillation and microcreep results obtained during the 47-h exposure of specimen 6261 to 1300 °C during run 890 (Fig. 8). The lack of such temporal evolution for specimen 6268 (see below) suggests that time-dependent

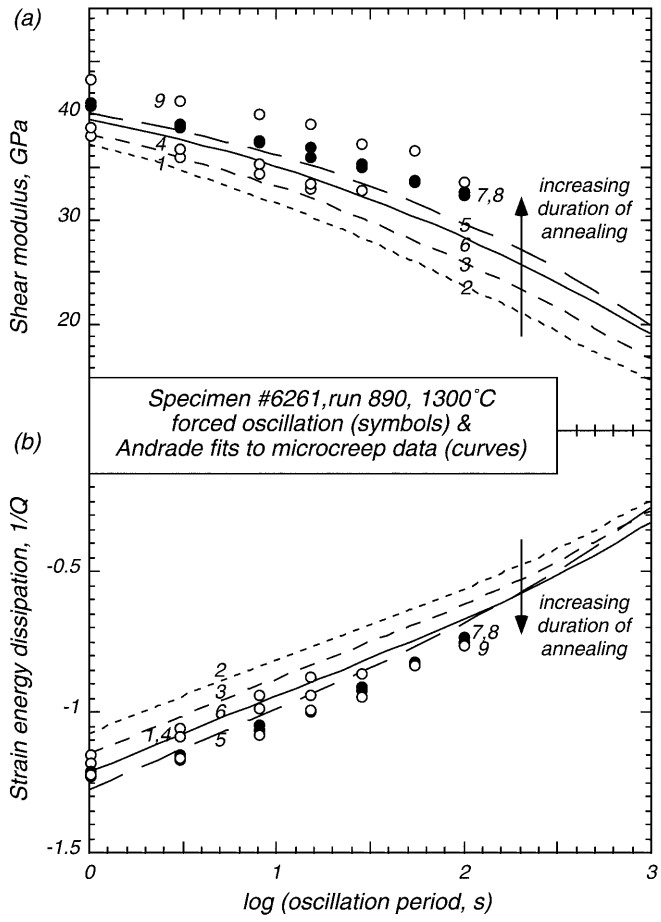

Fig. 8a, b Comparison of forced-oscillation (*plotting symbols*) and microcreep (*curves*) determinations of **a** shear modulus and **b** dissipation for tests 890-1 to 890-9 made consecutively over a period of 47 h at 1300 °C (Table 2). These plots highlight the broad consistency between forced-oscillation and microcreep information and also the systematic temporal evolution of the behaviour of specimen 6261 at 1300 °C

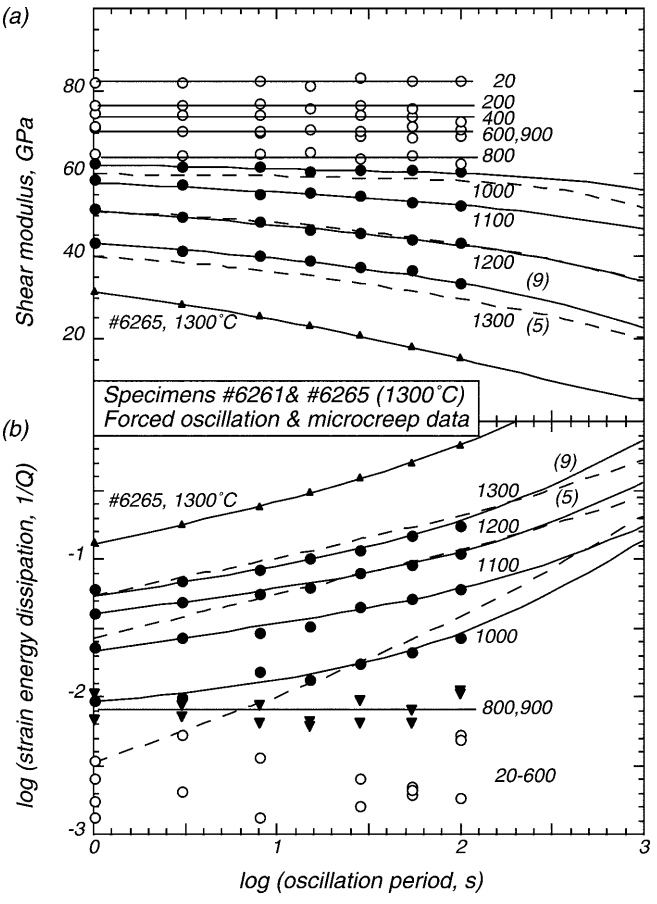

Fig. 9a, b A summary of all data obtained during the final staged cooling of specimen 6261 from 1300 °C, along with 1300 °C forced-oscillation data for the similarly prepared specimen 6265 (Tan et al. 1997a). Forced-oscillation data are indicated by the *plotting symbols* (*filled* and *open* for the viscoelastic and essentially elastic regimes, respectively), with the *solid curves* representing the Andrade fits to the modulus dispersion **a** and the dissipation **b**. The Andrade fits to the microcreep data are indicated by the *broken curves*. *Numbers in parentheses* denote annealing time in hours

behaviour, where it is observed, must reflect the changing microstructure and properties of the specimen itself. That the underlying processes are strongly thermally activated is indicated by the absence of significant temporal evolution in the mechanical behaviour over a period of 20 h at 1100–1200 °C during the prior temperature excursion (run 889) on this specimen.

Frequency and temperature dependence of G and Q^{-1}

The results of the final forced-oscillation tests conducted at 1300 °C and during the subsequent staged cooling are assembled in Fig. 9, along with corresponding information from the microcreep tests. Strong, markedly frequency-dependent dissipation and pronounced modulus dispersion are characteristic of temperatures $T \geq 1000$ °C. Below 1000 °C, the material behaves nearly elastically, with relatively low levels of dissipation <0.01 and no measurable dispersion. In order to further illustrate the temperature dependence of the shear modulus, the data measured at the mid-range oscillation period of 8 s are compared in Fig. 10 with expectations for a dense (crack- and pore-free) Fo_{90} polycrystal based on single-crystal elasticity measurements (Isaak 1992). The shear modulus measured in the present study at low frequencies is clearly consistent with ultrasonic data from room temperature to about 900 °C, but becomes markedly more temperature-sensitive at higher temperatures. The enhancement of $|\partial G/\partial T|$ is itself frequency-dependent – being substantially greater at long periods than for short periods (Fig. 9a).

Taking advantage of the close approach to consistent power-law dependence of Q^{-1} upon oscillation period, we have used Eq. (5) to model simultaneously the frequency and temperature dependence. The resulting parameters for the temperature interval 1100–1300 °C and 1–100 s period are presented in Table 5, where it is evident that an activation energy of 410 ± 54 (2σ) kJ mol^{-1} for the representative relaxation rate is

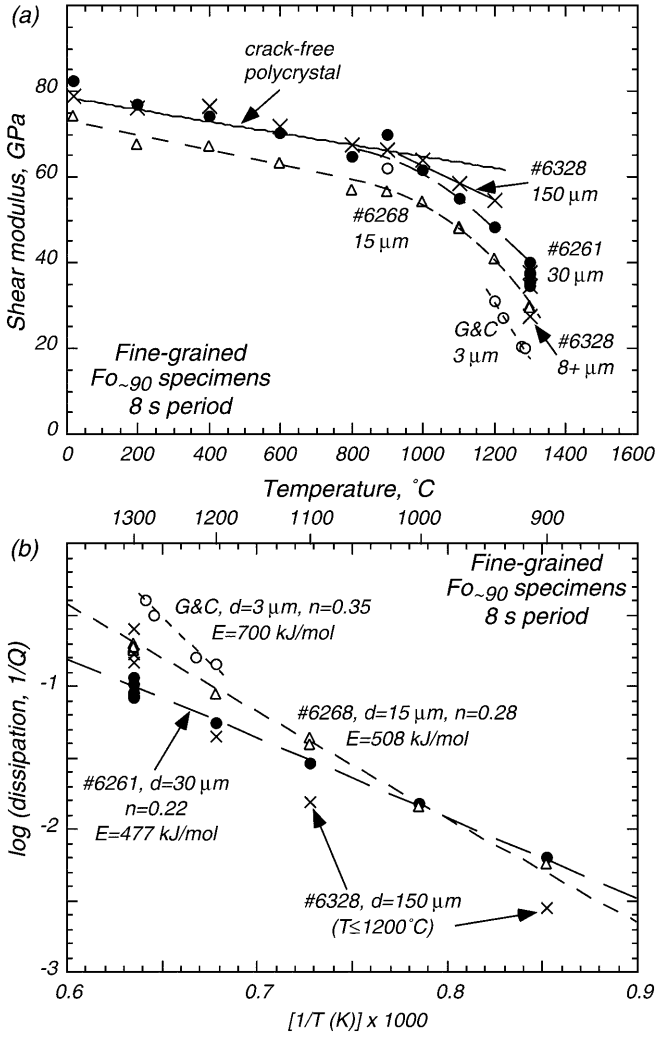

Fig. 10a, **b** Comparison of the forced-oscillation data obtained at the mid-range period of 8 s for the three specimens of the present study 6261 (*filled circles*), 6268 (*empty triangles*) and 6328 (*crosses*), and the synthetic dunite of 3 μm grain size (*empty circles*) from the study of Gribb and Cooper (1998). **a** Comparison of shear moduli measured in forced oscillation with the temperature-dependent average of the Hashin–Shtrikman bounds on aggregate G (labelled *crack-free polycrystal*) calculated from high-frequency (MHz) single-crystal data (Isaak 1992) for olivine of the same (Fo_{90}) composition. **b** Dissipation. The *long-* and *medium-dashed lines* for specimens 6261 and 6268, respectively, represent the Arrhenius fits (Eq. 5) of Table 5 evaluated at 8-s oscillation period. The *short-dashed line* represents the higher activation energy (700 kJ mol^{-1}) determined by Gribb and Cooper (1998)

combined with a power-law exponent of 0.23 ± 0.02. These parameters are relatively robust in the face of inclusion also of the 900–1000 °C data (Table 5; see also Fig. 10b).

Specimen 6268

The results of mechanical testing of specimen 6268, a texturally immature sample of distinctly bimodal grain size, prepared by hot-isostatic pressing of prefired 10–38 μm powder, are assembled in Table 3. Repeated testing over a 7-h exposure to 1300 °C at 200 MPa during the second thermal excursion for this specimen, and the results obtained in the preliminary thermal cycle, revealed no significant temporal evolution of its mechanical behaviour, in marked contrast to the results for specimen 6261 made from oven-dried powder of the same grain size. Compelling evidence for linearity[3] of the mechanical behaviour for peak shear strains below 10^{-5} was obtained from the insensitivity of G and Q^{-1} to variation of torque amplitude by a factor of 4 (forced oscillation tests 885-4-7 of Table 3). As for specimen 6261, strong frequency-dependent dissipation and accompanying dispersion are confined to temperatures ≥1000 °C (Fig. 11). General consistency is again observed between the inferences from forced-oscillation and microcreep tests.

Moduli determined on specimen 6268 during staged cooling are consistently lower for a given temperature than those for 6261 (Fig. 12a), and fall below the ultrasonic $G(T)$ trend well approximated by the data for 6261 for $T \leq 900$ °C (Fig. 10a). The greater residual porosity of specimen 6268 (Table 1) is presumably at least partially responsible for its consistent modulus deficit.

The variation of Q^{-1} with temperature and oscillation period for $1100 \leq T \leq 1300$ °C and $1 \leq T_0 \leq 100$ s is adequately described by Eq. (5) with an activation energy of 505 ± 64 (2σ) kJ mol^{-1} [somewhat higher than for 6261 (Fig. 10b)] and power-law exponent of 0.28 ± 0.03 (2σ) (Table 5).

Specimen 6328

Torsional forced-oscillation experiments and microcreep tests have also been carried out on HP6328 – an initially fine-grained specimen (~8 μm) prepared by hot-isostatic pressing of prefired 2–10-μm San Carlos olivine powder. Forced-oscillation measurements made after 2 h at 1300 °C during a preliminary run (no. 908) reveal the lowest moduli and highest dissipation measured in this study (Table 4; Fig. 13). The second excursion to high temperature (run 909) involved an additional 6.5 h annealing at 1300 °C, during which time three sets of forced-oscillation measurements and a microcreep test were conducted (Table 4). Very marked temporal evolution at 1300 °C was observed with a progressive reduction in dissipation accompanied by a systematic increase in modulus (Fig. 13). The final measurement at 1300 °C clearly indicates a modulus lower than for 6261, but this situation is reversed for all temperatures accessed during the subsequent staged cooling to room

[3] Linearity is defined by Nowick and Berry (1972, p.4) as follows: If a given stress history $\sigma_1(t)$ produces the strain $\varepsilon_1(t)$ and if a stress $\sigma_2(t)$ gives rise to $\varepsilon_2(t)$, then the stress $\sigma_1(t) + \sigma_2(t)$ will give rise to the strain $\varepsilon_1(t) + \varepsilon_2(t)$. Equivalently, it is required that the differential equation relating stress, strain and their respective time derivatives is of first degree (Nowick and Berry 1972, p 42).

Table 3 Andrade and extended Burgers rheologies fitted to torsional forced-oscillation[a] and microcreep[b] data for specimen 6268 tested in run 885 during a total of 7 h exposure to conditions of 1300 °C and 200 MPa, and during subsequent slow, staged cooling under pressure

Run no. Prior anneal[c] >h<	Model[d]	$\chi^{2(e)}$	$J_U/10^{-1}$ GPa^{-1}	Δ or $\beta/10^{-2}$ β: GPa^{-1} s^{-n}	α or n	log[τ_m (s)]	log[τ_M (s)]	$\eta/10^4$ GPa s
Temperature: 1300 °C								
885-2(O) 1.0	A-FeM	2.06	0.231(10)	1.15(10)	0.34(4)			0.19(6)
885-3(CV) 2.7	A-FePL	0.94	0.223(11)	1.76(12)	0.34(2)			0.26(7)
	B-FePL	0.94	0.251(6)	5.13(33)	0.34(2)	(−2)	(3)	0.22(5)
885-4(O)[f,g]4.6	A-FeM	6.39	0.230(15)	1.22(14)	0.32(5)			(0.19)
885-5(O)[f]5.3	A-FeM	0.17	0.231(15)	1.14(14)	0.32(5)			(0.19)
885-6(O)[h]6.0	A-FeM	0.17	0.227(26)	1.26(24)	0.28(8)			(0.19)
885-7(O)[f,i]6.5	A-FeM	0.31	0.230(16)	1.23(16)	0.31(5)			(0.19)
Temperature: 1200 °C								
885-8(O)	A-FeM	10.73	0.189(9)	0.62(10)	0.23(4)			1.01(50)
Temperature: 1100 °C								
885-9(O)	A-FeM	9.06	0.181(5)	0.28(5)	0.22(5)			4.73(491)
885-10(O)[j]	A-FeM	4.59	0.182(6)	0.28(6)	0.19(4)			(4.73)
Temperature 1000 °C								
885-11(O)	A-FeM	14.95	0.183(1)	0.044(6)	0.36(8)			15.00(2962)
885-12(CV)	A-FePL	0.22	0.189(1)	0.031(3)	0.44(5)			7.55(401)
	B-FePL	0.20	0.190(1)	0.212(48)	0.44(5)	(−2)	(3)	6.07(216)
Temperature: 900 °C								
885-13(O)	FeM	$\langle G\rangle^k = 56.48(37)$		$\langle Q^{-1}\rangle^k = 0.0065(18)$				
Temperature: 800 °C								
885-14(O)	FeM	$\langle G\rangle^k = 56.26(65)$		$\langle Q^{-1}\rangle^k = 0.0084(12)$				
Temperature: 600 °C								
885-15(O)	FeM	$\langle G\rangle^k = 63.40(40)$		$\langle Q^{-1}\rangle^k = 0.0019(7)$				
Temperature: 400 °C								
885-16(O)	FeM	$\langle G\rangle^k = 66.85(32)$		$\langle Q^{-1}\rangle^k = -0.0003(8)$				
Temperature: 200 °C								
885-17(O)	FeM	$\langle G\rangle^k = 67.10(18)$		$\langle Q^{-1}\rangle^k = -0.0002(5)$				
885-18(O)	FeM	$\langle G\rangle^k = 67.22(24)$		$\langle Q^{-1}\rangle^k = -0.0007(10)$				
Temperature: 20 °C								
885-19(O)	FePL	$\langle G\rangle^k = 74.32(25)$		$\langle Q^{-1}\rangle^k = 0.0005(11)$				

[a] Forced-oscillation data for periods of 1–100 s unless otherwise indicated
[b] Microcreep records of 5000 s total duration, comprising torque application and recovery intervals of 500 and 1500 s, respectively, processed to retrieve information concerning the response for periods of 1–305 s
[c] Prior exposure to 1300 °C, 200 MPa during present run; 2.5 h previous exposure during preliminary run (forced-oscillation data: 883-12) likewise shows little temporal evolution of the mechanical behaviour
[d] Significance of labels *A-FePL* and *A-FeM* as explained in Table 2
[e] Errors used in calculation as in Table 2
[f] 1–15 s
[g] Torque amplitude reduced by factor of 2
[h] 1–8 s
[i] Torque amplitude increased by factor of 2
[j] 1–28 s; additional ~9 h exposure
[k] Average values of G and Q^{-1} for $T \leq 900$ °C where dissipation and modulus dispersion are both small

temperature (Figs. 12c, 10a). Data for $T < 1000$ °C are indistinguishable from the ultrasonic trend (Fig. 10a).

Discussion

Quality of the new set of specimens

The olivine aggregates prepared here are significantly better for the purpose of measuring viscoelastic response than was the material for which we earlier presented preliminary results (Tan et al. 1997a). Improvements have been in several respects: (1) the reaction zone between specimen and jacket has been almost eliminated, and (2) effects of thermal microcracking have been significantly reduced by annealing for much longer times at 1300 °C prior to mechanical testing and by cooling at far slower rates during the return to room temperature.

Furthermore, the materials have been carefully characterised microstructurally using a range of methods. Although there are some undesirable features, such as mixed grain sizes, in different specimens, these characteristics have been fully documented. A very important feature is the overall low melt content, well below 0.1% in each specimen. The nature of GBs has been especially closely studied and the existence of Ca,Al impurities demonstrated on all GBs far removed from melt microstructures such as those at some triple-grain

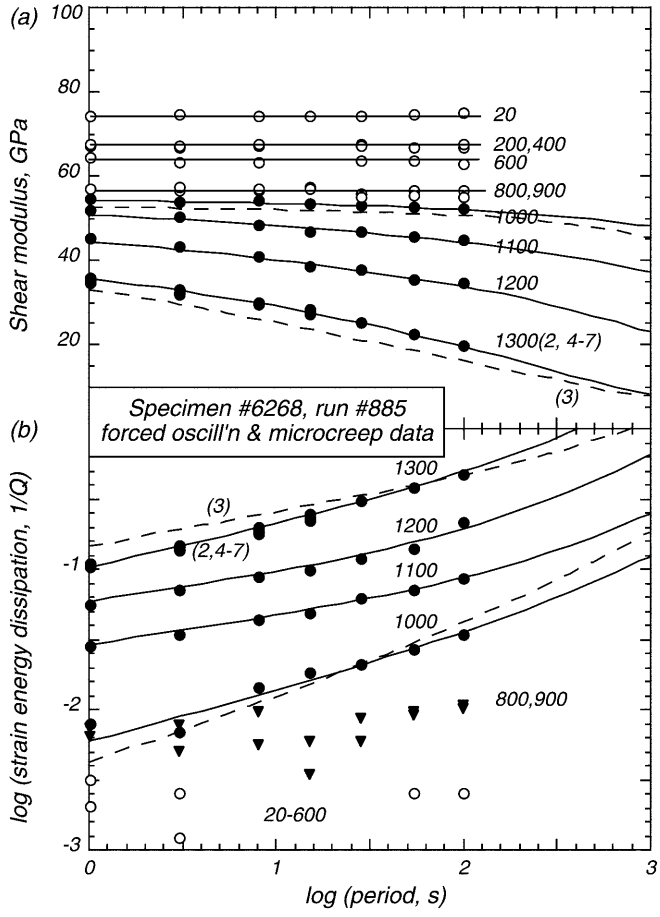

Fig. 11 **a** Shear modulus dispersion and **b** dissipation from forced-oscillation tests on specimen 6268 (Table 3). *Plotting symbols*, *curves* etc. as for Fig. 9. The close consistency among the results of forced-oscillation tests 885-2 and 885-4-7 and microcreep test 885-3 demonstrates the lack of significant temporal evolution of the behaviour of this specimen prepared from prefired coarse-grained (10–38 μm) powder

junctions. Calculations of phase equilibria (e.g. O'Neill and Wall 1987) involving olivine and the external metal foils suggest an oxygen fugacity f_{O_2} (presumably uniform throughout the samples of 12 mm diameter?) in the range 10^{-6}–10^{-7} Pa at 1300 °C and 200 MPa broadly consistent with the results of Raterron et al. (1998) amongst others. Similar calculations indicate that under these conditions all Cu should be present in the reduced state as observed, whereas most Zn should be oxidised and presumably accommodated in dilute (~0.1 mol%) solid solution in the olivine.

Microstructural basis for the observed mechanical behaviour

Specimen 6261

The very prolonged annealing (47 h) of specimen 6261 at 1300 °C and 200 MPa during its final excursion to high temperature was accompanied by substantial and systematic evolution towards higher modulus and lower dissipation (Fig. 8). Lower moduli and higher dissipation were measured during the preliminary excursions to high temperature (Table 2, note c). This strong sensitivity of the mechanical behaviour to the duration of prior annealing probably reflects a mixture of underlying microstructural changes. Amongst these are the healing of thermal microcracks, a modest amount of grain growth and associated progressive relaxation of intergranular stresses caused by anisotropic thermal expansion. The (mainly) diffusional mass transfer processes required for this relatively cryptic microstructural evolution may have been facilitated in this specimen by its water content which was initially substantial but decreased by almost 50% during the course of the mechanical testing (Table 1). Such microstructural evolution was presumably much more restricted in the similarly prepared specimen 6265 tested over a 3-h period following a 3-h anneal at 1300 °C by Tan et al. (1997a), explaining its substantially lower moduli and higher dissipation (Fig. 9). Indeed, these data for specimen 6265 are comparable with those obtained on specimen 6261 during its preliminary excursions to high temperature.

Mechanical testing during subsequent staged cooling to 900 °C reveals a strong systematic decrease in dissipation and associated recovery of the viscoelastic modulus defect (Figs. 9, 10). For temperatures ≤900 °C, the behaviour is essentially elastic with dissipation $<10^{-2}$ and negligible frequency dependence of the shear modulus. The moduli measured for the temperature interval 900–20 °C are indistinguishable within experimental error from the modulus-temperature trend calculated for a dense polycrystal from ultrasonic elasticity data for single-crystal olivine of the same composition (Fig. 10a). This observation is important because it demonstrates conclusively the absence of any significant amount of crack porosity. The mechanical behaviour measured in the final tests at 1300 °C and during the subsequent staged slow cooling under pressure is therefore associated unambiguously with uncracked polycrystalline Fo_{90} of 30 μm average grain size. These results are accordingly regarded as a yardstick against which the behaviour of the somewhat more complicated materials 6268 and 6328 can instructively be compared (Figs. 10, 12).

That thermal microcracking was only barely suppressed during the cooling under pressure of specimen 6261 is evident from the previously mentioned progressive cracking observed in the AT6261 thin section corroborated by the low elastic wavespeeds (Table 1, note c) measured in bench-top ultrasonic measurements conducted some months later.

Specimen 6328

The hot-pressed specimen HP6328 is uniformly fine-grained (average grain size 8 μm). Microcracks are few

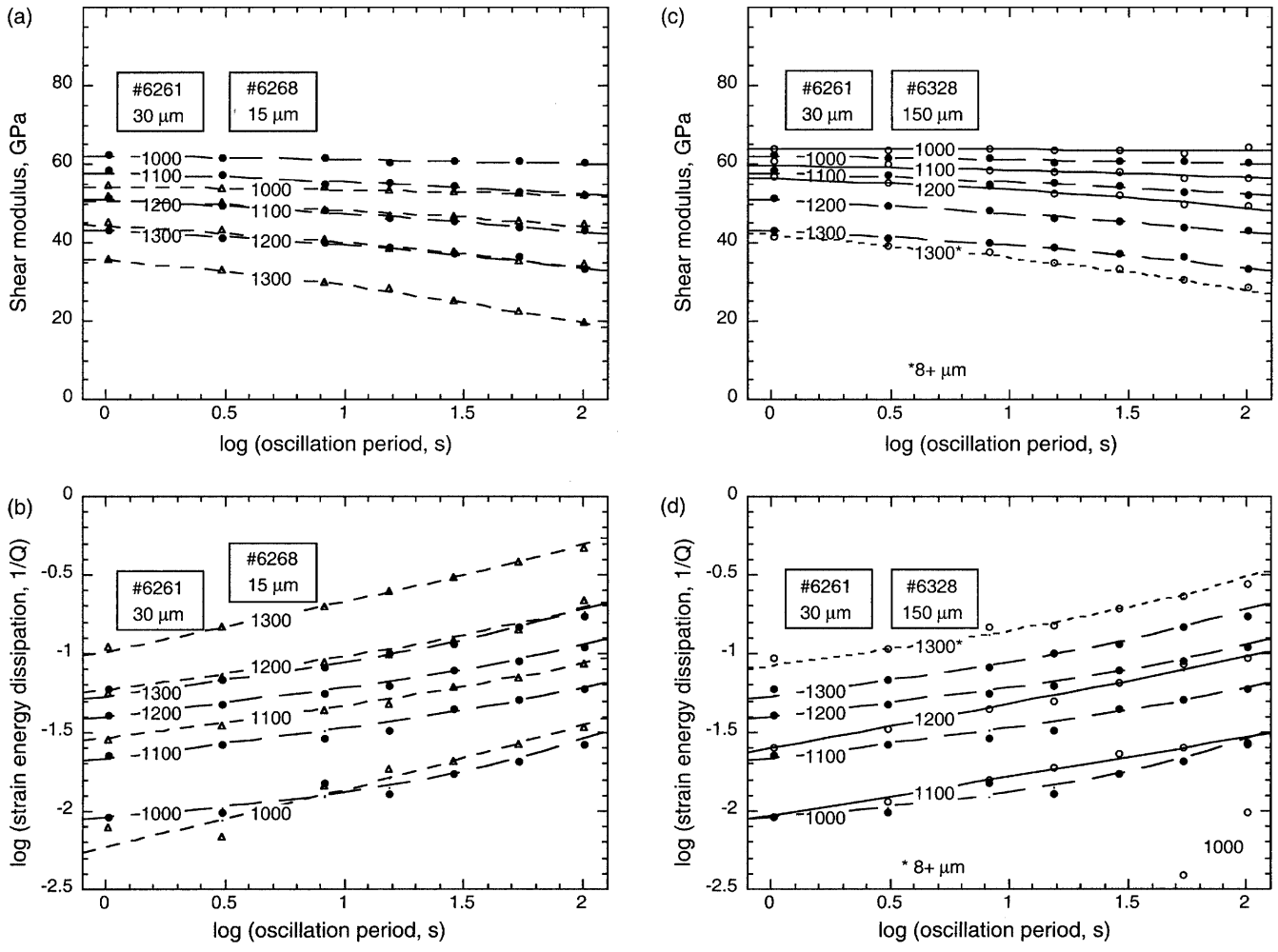

Fig. 12a–d Comparison of the results of forced-oscillation tests conducted during staged cooling of the three polycrystalline olivine specimens across the interval 1300–1000 °C. **a** Modulus dispersion and **b** dissipation for specimens 6261 (*filled circles*, *long-dashed curves*) and 6268 (*empty triangles* and *short-dashed curves*). **c** Modulus dispersion and **d** dissipation for specimens 6261 (*as above*) and 6328 (*empty circles* and *very short-dashed* (1300 °C) *or continuous* (≤1200 °C) *curves*). The *dash lengths* for the various specimens thus mirror the variation in grain size

in thin section, and bench-top ultrasonic wave speeds are closely comparable with those for an ideal polycrystal (Table 1, note e). The small grain size of this specimen is presumably responsible for the scarcity of microcracks. Notwithstanding these attractive properties, the mechanical behaviour of this specimen, like the more coarse-grained 6261 was found to evolve systematically with the duration of annealing at 1300 °C and 200 MPa (Fig. 13). The final measurement on specimen 6328 at 1300 °C shows it to be lower in modulus and more lossy than specimen 6261 under the same conditions, but this situation is reversed for lower temperatures within the viscoelastic regime (1200–1000 °C) where 6328 is systematically higher in modulus and less lossy than 6261 (Figs. 10, 12). For $T \leq 1000$ °C, specimen 6328 exhibits essentially elastic behaviour with a close approach to the $G(T)$ trend expected for a dense polycrystal (Fig. 10a). It is therefore concluded, as for specimen 6261, that thermal microcracking was effectively suppressed during the staged slow cooling to room temperature under 200 MPa pressure.

Examination of thin sections cut from the specimen AT6328 implicated abnormal grain growth (to ~150 μm average grain size) as the cause of the anomalous behaviour (Fig. 4b). Moreover, the observation at temperatures of 1000–1200 °C of higher moduli and lower dissipation than for specimen 6261 of 30 μm average grain size, and the reversal of this relationship at 1300 °C (Figs. 10, 12), strongly suggest that the high-temperature viscoelastic behaviour must be grain-size-sensitive. Surprisingly, however, this interpretation requires most of the grain growth to have occurred during the ~40 min cool from 1300 to 1200 °C and the subsequent 140 min hold at 1200 °C prior to test 909-5. Perhaps grain growth, already underway and manifest in the temporal evolution of mechanical behaviour at 1300 °C, was exacerbated by the thermal stresses associated with cooling. Also somewhat remarkable is the fact that this specimen was recovered along the crack-free G(T) trend notwith-

Table 4 Andrade and extended Burgers rheologies fitted to torsional forced-oscillation[a] and microcreep[b] data for specimen 6328 tested in runs 908 and 909 during a total of 12 h exposure to conditions of 1300 °C and 200 MPa, and during subsequent slow, staged cooling under pressure

Run no. Prior anneal[c] > h <	Model[d]	$\chi^{2(e)}$	$J_U/10^{-1}$ GPa^{-1}	Δ or $\beta/10^{-2}$ β: $GPa^{-1}\ s^{-n}$	α or n	$\log[\tau_m\,(s)]$	$\log[\tau_M\,(s)]$	$\eta/10^4$ GPa s
Temperature: 1300 °C								
908-7(O) 2.5	A-FeM	4.46	0.231(15)	1.49(15)	0.31(4)			0.086(17)
< inadvertent rapid cool to room temperature >								
909-2(O) 6.5	A-FeM	13.03	0.208(12)	0.99(12)	0.28(4)			0.28(9)
909-3(CV) 8.0	A-FePL	0.29	0.213(8)	1.10(8)	0.33(2)			0.70(32)
	B-FePL	0.27	0.231(4)	3.3(2)	0.33(2)	(−2)	(3)	0.55(18)
909-4(O) 10.0	A-FeM	8.21	0.187(13)	0.91(14)	0.24(4)			0.41(13)
< 40 min cool to 1200 °C, then 2 h 20 min wait prior to data acquisition >								
Temperature: 1200 °C								
909-5(O)	A-FeM	5.15	0.168(3)	0.191(27)	0.293(51)			7.8(145)
909-6(CV)	A-FePL	0.03	0.171(2)	0.147(15)	0.34(3)			6.4(44)
	B-FePL	0.02	0.174(1)	0.631(70)	0.34(3)	(−2)	(3)	4.6(21)
< held overnight at 1140 °C >								
Temperature: 1100 °C								
909-7(O)	A-FeM	9.55	0.164(1)	0.071(9)	0.253(28)			(100)
909-8(CV)	A-FePL	0.35	0.165(1)	0.040(3)	0.405(23)			(100)
	B-FePL	0.23	0.165(1)	0.275(48)	0.415(44)	(−2)	(3)	36.3(591)
Temperature: 1000 °C								
909-9(O)	FeM	$\langle G\rangle^{f}$ =	63.68(43)	$\langle Q^{-1}\rangle^{f}$ =	0.0022(29)			
Temperature: 900 °C								
909-10	FePL		66.45(34)		0.0019(20)			
Temperature: 800 °C								
909-11	FePL		66.80(95)		0.0130(17)			
Temperature: 600 °C								
909-12	FePL		72.05(22)		0.0032(22)			
Temperature: 400 °C								
909-13	FePL		76.73(47)		0.0016(10)			
Temperature: 200 °C								
909-14	FePL		75.77(29)		0.0006(12)			
Temperature: 20 °C								
909-15[g]	FePL		78.82(1)		0.0012(25)			

[a] Forced-oscillation data for periods of 1–100 s unless otherwise indicated
[b] Microcreep records of 5000 s total duration, comprising torque application and recovery intervals of 500 and 1500 s, respectively, processed to retrieve information concerning the response for periods of 1–305 s
[c] Prior exposure to 1300 °C and 200 MPa during runs 908 and 909; the specimen was inadvertently cooled relatively rapidly (within ~30 min) to room temperature and reheated to 1300 °C between 908-7 and 909-2
[d] Significance of labels *A-FePL* and *A-FeM* etc. as for Table 2
[e] Errors used in calculation of χ^2 as for Table 2
[f] Average values of G and Q^{-1} for $T \leq 1000$ °C where dissipation and modulus dispersion are both small
[g] 1–15 s

standing its (final) large grain size (150 μm) and evidence in thin section for pervasive microcracking. It must be concluded that the confining pressure of 200 MPa was barely sufficient to inhibit thermal microcracking during cooling under pressure, and that the microcracking occurred during the subsequent depressurisation.

It is tempting to associate the abnormal grain growth in specimen 6328 with possible reintroduction of water to the dry hot-pressed specimen during the water-cooled precision grinding of the cylindrical specimen for mechanical testing (Table 1). However, the same opportunity for reintroduction of water into a relatively dry, but more coarse-grained specimen, existed for 6268 where textural equilibration appears to have been much more sluggish (see below).

Specimen 6268

Specimen 6268 differs from 6261 and 6328 in showing no significant temporal evolution of its mechanical behaviour during a total of 10 h annealing at 1300 °C (Table 3; Fig. 11). There is also no significant grain-

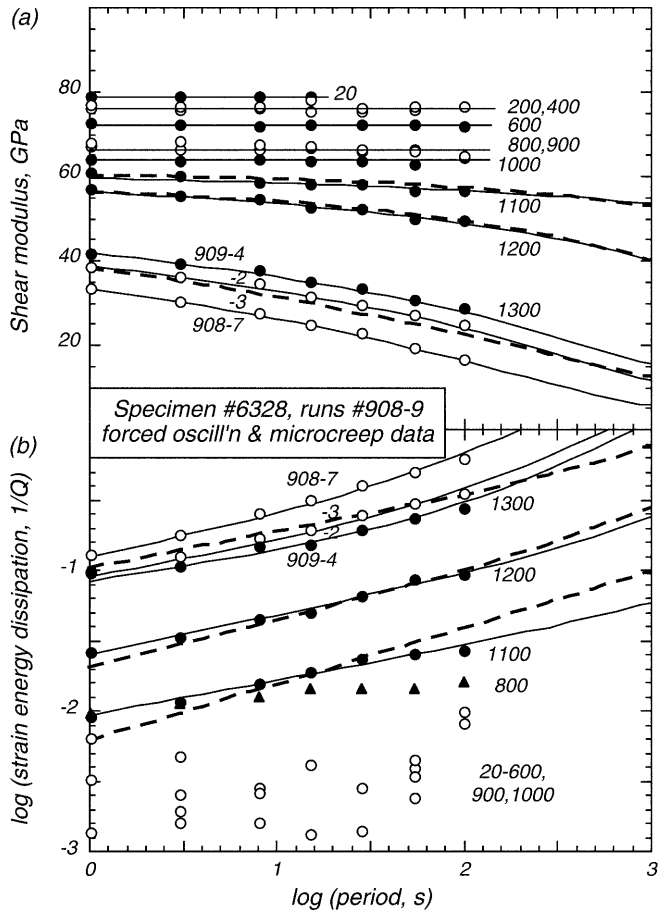

Fig. 13 a Shear modulus dispersion and **b** dissipation from forced-oscillation tests on specimen 6328 (Table 4). *Plotting symbols*, *curves*, *etc*. generally as for Fig. 9, but with *open symbols* used here both for early forced-oscillation tests at 1300 °C, and for alternate temperatures below 1000 °C. The results of tests 908-7 and 909-2 to 4 at 1300 °C reveal a systematic trend with time towards higher modulus and lower dissipation

scale microstructural evolution evident in thin section with a markedly bimodal distribution of grain size (Fig. 5, average grain size 15 μm) surviving the annealing without significant grain growth. Presumably, the dryness of this specimen prepared from prefired powder must be responsible for its lack of microstructural evolution – although, as noted above, the same consideration should reasonably have applied to specimen 6328.

Comparison of the mechanical behaviour for specimen 6268 with that for specimen 6261 reveals systematically substantially lower moduli and higher dissipation for 6268 at temperatures of 1100–1300 °C (Fig. 12). These observations are consistent with the notion of grain-size-sensitive viscoelastic behaviour, with higher dissipation and more strongly dispersed moduli for the more fine-grained material. At 1000 °C, the two specimens display comparable levels of dissipation but 6268 is decidedly lower in modulus; this trend persists throughout the temperature interval 1000–20 °C (Fig. 10a). As for the other specimens, the behaviour is essentially elastic for $T \leq 900$ °C but the consistently lower shear moduli, diagnostic of significant porosity, are attributed mainly to porosity residual from the hot-isostatic pressing (1.9% – Table 1).

Grain-size-sensitive viscoelastic relaxation

Strain energy dissipation and modulus dispersion

Many variables, including trace amounts of melt, the Cu-rich and Ni–Fe metallic impurities, dislocation density and especially [H_2O] (e.g. Karato and Jung 1998), have the potential to significantly influence the mechanical behaviour. However, it appears from Figs. 10a and 14 that most of the observed variation in dissipation and modulus dispersion for the three specimens of this study is attributable to variation in grain size (Tan et al. 1997b). This conclusion is reinforced by the results of a subsequent study in progress in our laboratory in which olivine polycrystals have been fabricated from both natural (San Carlos) and synthetic (sol-gel) precursors under more oxidising conditions provided by encapsulation in $Ni_{70}Fe_{30}$ containers. No evidence has been found to suggest that reducing conditions (responsible for the Ni–Fe blebs in the specimens of the present study) or the presence of Cu impurities (consequent upon sieving the crushed San Carlos olivine) significantly influence the measured mechanical behaviour.

The $Q^{-1}(T_0)$ trends at 1100 and 1200 °C for specimens 6328 ($d = 150$ μm, following abnormal grain growth), 6261 ($d = 30$ μm) and 6268 ($d = 15$ μm) reveal a systematic increase of dissipation with decreasing grain size (Fig. 14b, c). Accordingly, the fact that the dissipation measured at 1300 °C on specimen 6328 is intermediate between the $Q^{-1}(T_0)$ trends for 6268 (15 μm) and 6261 (30 μm) (Fig. 14a) suggests an average grain size between 15 and 30 μm at the time of the final testing at 1300 °C – consistent with the occurrence of substantial prior grain growth (from the initial average grain size of 8 μm). The dissipation measured by Gribb and Cooper (1998) on a reconstituted dunite is greater than Q^{-1} for the polycrystalline olivine specimens of the present study (Fig. 14), consistent with its substantially smaller grain size (3 μm).

The inference that the high-temperature viscoelastic behaviour is grain-size sensitive is reinforced by trends evident among the modulus data plotted in Fig. 10a. The shear modulus measured at each temperature in the range 1000–1300 °C decreases systematically with decreasing grain size, as the result of progressively stronger viscoelastic relaxation. Substantially lower values of the shear modulus were measured on the reconstituted dunite of Gribb and Cooper (1998) in accord with its much smaller grain size (Fig. 10a).

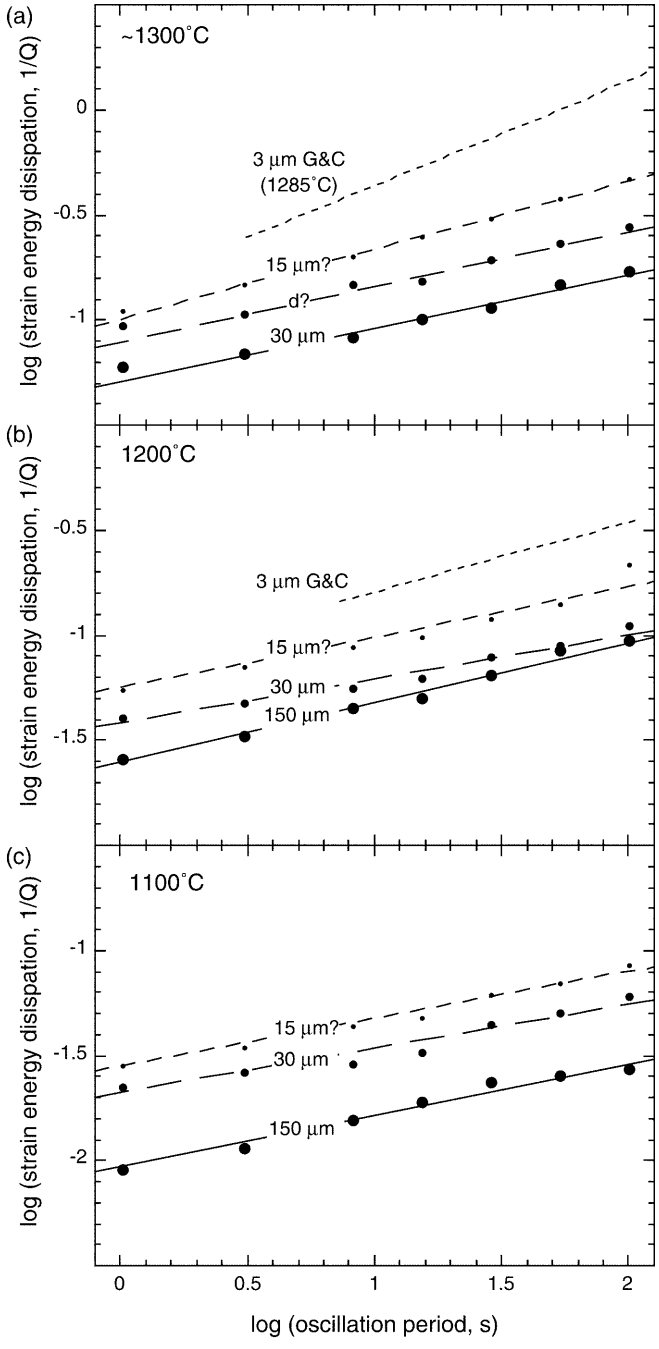

Fig. 14a–c Comparison of dissipation versus oscillation period data for specimens 6261, 6268 and 6328 of the present study and the reconstituted dunite of Gribb and Cooper (1998) highlighting the systematic variation with grain size. At each temperature: **a** ~1300 °C; **b** 1200 °C and **c** 1100 °C, plotting symbols of different sizes and curves ranging from *unbroken* through *long-dashed*, *medium-dashed* and *short-dashed* are used to represent the data for specimens 6261 (grain size $d = 30$ μm), 6268 ($d = 15$ μm), 6328 [$d > 8$ μm (1300 °C), $d = 150$ μm (≤1200 °C)]. The data of Gribb and Cooper (1998) for a reconstituted dunite of 3-μm grain size are labelled *G* & *C*

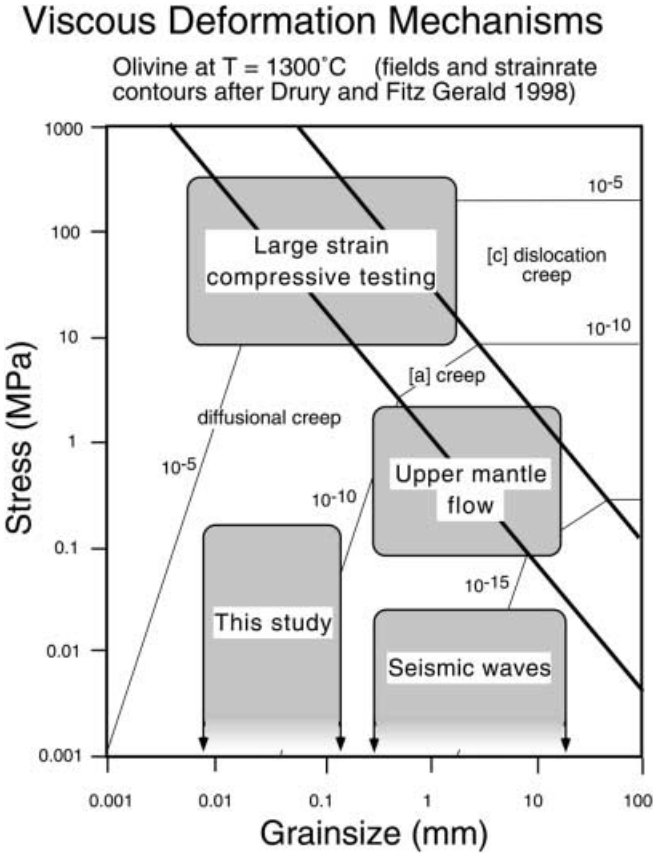

Fig. 15 Deformation mechanism map for polycrystalline Fo_{90} olivine at 1300 °C (after Drury and Fitz Gerald 1998, Fig. 11.7a). The grain-size-stress field for the mechanical tests of the present study ($8 < d < 150$ μm, $\sigma < 0.15$ MPa) falls squarely within the field in which diffusional creep dominates over steady-state dislocation creep

Steady-state viscosity

Some circumstantial support for the notion that the viscoelastic (sensu lato) behaviour responsible for the dissipation and modulus dispersion observed in the present study is grain-size sensitive can be drawn from consideration of the deformation mechanism map for steady-state creep in olivine (Fig. 15). At the representative temperature of 1300 °C the conditions of stress and grain size pertaining to the tests of this study fall squarely within the field in which diffusional creep dominates over dislocation creep. More significantly, the steady-state viscosities inferred from the forced-oscillation and microcreep data (Tables 2, 3, 4) vary systematically with grain size. At 1300 °C, the viscosities associated with Andrade and Burgers fits to the microcreep data for specimens 6261 and 6268 are respectively (0.9–1.9) × 10^{13} Pa s and (0.2–0.3) × 10^{13} Pa s. The ~six fold contrast in viscosity for a two fold difference in mean grain size d is consistent with expectations for diffusional creep whereby $\eta \sim d^2$ for Nabarro–Herring creep (lattice diffusion controlled) or d^3 for Coble creep (grain-boundary diffusion controlled; e.g. Frost and Ashby 1982). The corresponding viscosity for specimen 6328 is (0.6–0.7) × 10^{13} Pa s (Table 4), intermediate between those for the other two specimens and consistent with the notion developed above that its grain size at that stage of the mechanical testing was between 15 and 30 μm.

Comparison with viscosity determined in large-strain compressive tests

The viscosities inferred from the microstrain torsional tests of the present study can be compared instructively with those calculated from flow laws for diffusional creep in olivine derived from conventional large-strain compressive deformation experiments (e.g. Hirth and Kohlstedt 1995; Drury and Fitz Gerald 1998). For example, for 30 μm grain size, 1300 °C and the f_{O_2} of the Fe–FeO buffer, the flow law for diffusional creep in dry olivine, suitably adjusted to the stress state of torsional testing (Jackson 2000), yields a viscosity η of 5×10^{13} Pa s, which is just half an order of magnitude greater than that determined for specimen 6261 in the torsional microcreep tests 890-5 and 890-6 of Table 2.

Possible explanations for this admittedly relatively small difference in viscosity include differing H_2O contents and a reduced viscosity for the Ca,Al-rich impurity regions at grain boundaries. Specimen AT6261 with 130 ppm H_2O contains at least ten times more water than the dry melt-free specimens of Hirth and Kohlstedt (1995). The ~30-fold contrast in viscosity between dry and wet olivine deformed at 1300 °C by diffusional creep (Karato et al. 1986; Drury and Fitz Gerald 1998) suggests that the difference of half an order of magnitude inferred above could readily be attributed to the trace amount of water in AT6261. Alternatively, enhanced deformation of narrow, potentially low-viscosity GB regions with interlocked grain geometry, although limited to very small strains, might contribute significantly at the microstrains of the present torsional tests, resulting in a reduction of the viscosity. At the much larger strains (~10%) of conventional compressive tests, this contribution would be negligible, resulting in a higher viscosity.

Frequency and grain-size dependence of dissipation: implications for relaxation mechanisms

The microcreep tests of the present study and that of Gribb and Cooper (1998) provide clear evidence that the high-temperature viscoelastic behaviour involves a mixture of recoverable (anelastic) and irrecoverable (viscous) contributions. If this were not so, and the non-elastic deformation were entirely viscous in nature, a Maxwell rheology would apply with frequency (ω) and grain size (d) sensitivity of the dissipation given by

$$Q^{-1} = (\omega \eta J_U)^{-1} \propto T_0 d^{-m} \quad , \tag{9}$$

with $m = 2$ for Nabarro–Herring creep or $m = 3$ for Coble creep. Both the frequency and grain-size sensitivity observed in this study are much milder than these simple considerations would imply. For periods of 1–100 s and grain sizes of 8–150 μm the dissipation varies as $Q^{-1} \propto T_0^{\alpha} d^{-m}$ with $\alpha \sim 0.2$–0.3, and $m < 0.5$ (see especially Fig. 14b, c).

The grain-size-sensitive diffusional creep revealed by the 1300 °C microcreep tests indicates that grain-scale diffusion (probably mainly along grain boundaries) occurs on timescales of 1000–10 000 s. Timescales τ and spatial scales x for diffusion are quite generally related by the expression $\tau = x^2/D$, where D is the appropriate diffusivity. It therefore follows that for spatial scales $(0.001–0.1) \times d$ much smaller than the grain size, much shorter diffusional timescales (0.001–100 s) are to be expected. The local viscous flow within the grain-boundary region of <10 nm effective thickness that is required to relax boundary shear stresses and thereby allow grain-boundary sliding, is accordingly expected to occur during mechanical testing even at periods <1 Hz. It is concluded that elastically accommodated grain-boundary sliding with its large relaxation strength (~30%, Raj and Ashby 1971) is likely to account for much of the anelastic deformation that dominates the non-elastic response at short periods and moderate temperatures in the present study. At sufficiently high temperatures, the effect of increasing period (across the range 10–10 000 s at 1300 °C in the present study) is to allow diffusional accommodation on progressively larger spatial scales to become dominant over the elastic accommodation that guarantees recoverability of the strain at short periods. The consequence is a seamless transition into the viscous behaviour associated with diffusionally accommodated grain-boundary sliding (Raj 1975; Gribb and Cooper 1998).

Temperature dependence of diffusional processes in Fo_{90} olivine: activation energies

The notion that the processes (both anelastic and viscous) responsible for the measured dissipation are diffusional in origin gains some additional credence from the similarities between the activation energies inferred in this study (Table 5) and those for diffusional creep and for the diffusion of the relevant defect species. From diffusional creep measurements over the narrow temperature interval 1200–1250 °C, Hirth and Kohlstedt (1995) inferred an activation energy of 315 ± 35 kJ mol^{-1}, but apparently preferred a value near 350 kJ mol^{-1} obtained by averaging their result with that derived from previous observations of densification of olivine aggregates. The activation energies obtained in the present study are consistently between 400 and 500 kJ mol^{-1} (Table 5), with the value of 410 ± 54 (2σ) kJ mol^{-1} for the texturally well-equilibrated specimen (6261) of stable grain size at temperatures of 1100–1300 °C regarded as the most robust. A higher activation energy of 525 kJ mol^{-1} has been inferred for multicomponent lattice diffusion in Fo_{90} olivine (Jaoul 1990). However, activation energies for grain-boundary diffusion are typically significantly lower than those for lattice diffusion (e.g. Frost and Ashby 1982).

The markedly higher activation energy (700 kJ mol^{-1}) determined by Gribb and Cooper (1998) is probably

Table 5 Fits of the expression $Q^{-1} = AT_0^n \exp(-nE/RT)$ to the period and temperature dependence of Q^{-1} as determined in forced-oscillation tests for periods of 1–100 s on the olivine polycrystals 6261 and 6268 of the present study and 6265 of Tan et al. (1997a). *Numbers in parentheses* are 1σ uncertainties in the last significant figure

Specimen no.	Temperature (°C)	N	A (10^2)	n	E (kJ mol^{-1})	RMS misfit (%)
6265	1100–1300	27	28.3(70)	0.31(1)	420(15)	6.2
6261	1100–1300	21	0.66(21)	0.23(1)	410(27)	7.2
	900–1300	32[a]	2.14(43)	0.22(2)	477(32)	10.8
6268	1100–1300	21	50.9(202)	0.28(2)	505(32)	9.3
	1000–1300	26[b]	60.7(146)	0.28(2)	508(25)	8.8

[a] 1, 3-s data at 900 °C and 1 s datum at 1000 °C excluded
[b] 1, 3-s data at 1000 °C excluded

attributable to the much higher level of Ca,Al impurities in their reconstituted dunite specimen – either directly through the influence of impurity segregations upon grain-boundary diffusivity (Gribb and Cooper 1998) or indirectly through the influence of a small and temperature-dependent melt fraction.

Future directions

The less than ideal microstructural behaviour/characteristics of specimens 6268 and 6328 preclude a definitive quantitative analysis at this stage of the grain-size sensitivity of the dissipation and its mechanistic implications. The nature of the microstructure of specimen 6268 (Fig. 5a) casts doubt on the quantitative significance of its 15-μm average grain size. Instead, its behaviour in the grain-size-sensitive regime may well be determined by grain size in the rim of smaller grains that typically envelops the larger grains. For specimen 6328, the marked grain growth introduces uncertainty, especially concerning the grain size to be associated with the 1200 and 1300 °C data.

Quantitative analysis of the grain-size sensitivity and the roles of other potentially important variables such as $[H_2O]$ and f_{O_2} must await the results of work in progress on additional specimens being prepared from both natural (San Carlos) and synthetic sol-gel precursors, and being fabricated and tested within the more oxidising environment provided by Ni–Fe containers. Only then will it be possible to apply the laboratory findings with any confidence in the interpretation of the seismological models for the variation of wavespeeds and attenuation in the Earth's upper mantle.

Conclusions

This study represents a substantial extension of our previous work (Tan et al. 1997a) on seismic shear wave dispersion and dissipation at high temperature in fine-grained olivine polycrystals and synthetic dunites. The new study has involved the fabrication, characterisation and low-strain torsional mechanical testing of a suite of Fo_{90} olivine polycrystals. The chemical environment in which the specimens were tested has been simplified through the use of pure Fe foil to isolate the specimen from the mild steel jacket. Significant improvements to the experimental procedure include longer periods of high-temperature annealing and slower cooling during the subsequent return to room temperature, and the conduct along with the forced-oscillation experiments of a larger number of complementary microcreep tests. In addition, the specimens have been thoroughly characterised microstructurally. They range in mean grain size from 8 to 150 μm, are all of very low porosity (<2%), and display generally low but somewhat variable dislocation densities. Importantly, they contain only trace amounts (≪0.1 vol%) of glass representing quenched melt.

For these reasons, the present study provides the most robust constraints yet available on the high-temperature low-strain viscoelastic behaviour of essentially melt-free polycrystalline olivine, as follows:

1. The high quality and slow cooling of specimens 6261 and 6328 has allowed their recovery along $G(T)$ trajectories for $T < 900$ °C closely consistent with expectations from single-crystal elasticity data. This comparison confirms essentially elastic behaviour below 900 °C uncomplicated by thermal microcracking, which has plagued previous experiments especially on more coarse-grained materials.
2. The closely consistent and complementary results of torsional forced-oscillation and microcreep tests are indicative of linear, markedly viscoelastic behaviour at temperatures ≥1000 °C and seismic frequencies (mHz–Hz). Within a broad absorption band Q^{-1} varies with frequency and temperature as $\omega^{-\alpha} \exp(-\alpha E/RT)$ with $0.2 < \alpha < 0.3$ and $400 < E < 500$ kJ mol^{-1}.
3. The measured dissipation Q^{-1} and modulus dispersion $G(\omega)$ provide clear indications of grain-size sensitivity of the viscoelastic behaviour – both increasing with decreasing grain size. Although the grain-size sensitivity remains to be robustly quantified, it is clearly milder than previously suggested. The exponent m in the relationship $Q^{-1} \sim d^{-m}$ is apparently <0.5 rather than ~1 as assumed in recent tentative extrapolations to mantle grain sizes (Gribb and Cooper 1998; Jackson 2000).
4. In addition to the grain-size sensitivity, several lines of evidence suggest that diffusional processes are

responsible for both the anelastic and viscous components of the viscoelastic behaviour. Dislocation densities, although somewhat variable, are generally low. The conditions of stress, temperature and grain size explored in this study fall well within the diffusional creep field on the deformation mechanism map for steady-state creep. Moreover, steady-state viscosities associated with fits to the microcreep data are comparable with those determined for diffusional creep in large-strain compressive testing. Finally, the activation energies, plausibly associated with rate-controlling grain-boundary diffusion, observed for the relaxation responsible for the dissipation measured in the present study are not markedly dissimilar from those for diffusional creep.

5. The non-elastic strain observed at high temperatures and seismic frequencies is a mixture of recoverable (anelastic) and permanent (viscous) contributions, probably attributable mainly to elastically accommodated and diffusionally accommodated grain-boundary sliding, respectively. The proportion of viscous deformation increases monotonically with increasing temperature and decreasing frequency.

Acknowledgements We thank Graeme Horwood for maintenance of the laboratory equipment and Harri Kokkonen for assistance with specimen preparation. Wayne Taylor, Andrew Berry and Nerilie Abram are thanked for help with the infrared spectroscopy and Melissa Ehrlich for the ultrasonic measurements. Benhua Tan thanks the Research School of Earth Sciences, ANU, for scholarship support. The manuscript was significantly improved in response to the comments of an anonymous reviewer.

References

Berckhemer H, Kampfmann W, Aulbach E, Schmeling H (1982) Shear modulus and Q of forsterite and dunite near partial melting from forced-oscillation experiments. Phys Earth Planet Inter 29: 30–41

Brennan BJ, Smylie DE (1981) Linear viscoelasticity and dispersion in seismic wave propagation. Rev Geophys Space Phys 19: 233–246

Brown GE Jr (1980) Olivines and silicate spinels. In: Ribbe PH (ed) Orthosilicates. Mineral Soc Am, Washington, DC, pp 275–365

de Kloe R, Drury MR, van Roermund HLM (2000) Evidence for stable grain boundary melt films in experimentally deformed olivine-orthopyroxene rocks. Phys Chem Miner 27: 480–494

Drury MR, Fitz Gerald JD (1996) Grain boundary melt films in an experimentally deformed olivine-orthopyroxene rock: implications for melt distribution in upper mantle rocks. Geophys Res Lett 23: 701–704

Drury MR, Fitz Gerald JD (1998) Mantle rheology: insights from laboratory studies of deformation and phase transition. In: Jackson I (ed) The Earth's mantle: composition, structure and evolution. Cambridge University Press, New York, pp 503–559

Durek J, Ritzwoller MH, Woodhouse JH (1993) Constraining upper mantle anelasticity using surface wave amplitude anomalies. Geophys J Int 114: 249–272

Dziewonski AM, Anderson DL (1981) Preliminary reference Earth model. Phys Earth Planet Int 25: 297–357

Frost HJ, Ashby MF (1982) Deformation-mechanism maps: the plasticity and creep of metals and ceramics. Pergamon Press, Oxford, 166 pp

Goetze C (1977) A brief summary of our present day understanding of the effect of volatiles and partial melt on the mechanical properties of the upper mantle. In: Manghnani MH, Akimoto S (eds) High-pressure research: applications in geophysics. Academic Press, New York, pp 3–23

Grand SP (1994) Mantle shear structure beneath the Americas and surrounding oceans. J Geophys Res 99: 11 591–11 621

Grand SP, Helmberger DV (1984) Upper mantle shear structure of North America. Geophys J Rastron Soc 76: 399–438

Gribb TT, Cooper RF (1998) Low-frequency shear attenuation in polycrystalline olivine: grain-boundary diffusion and the physical significance of the Andrade model for viscoelastic rheology. J Geophys Res 103: 27 267–27 279

Gueguen Y, Darot M, Mazot P, Woirgard J (1989) Q^{-1} of forsterite single crystals. Phys Earth Planet Int 55: 254–258

Hirth G, Kohlstedt DL (1995) Experimental constraints on the dynamics of the partially molten upper mantle: deformation in the diffusion creep regime. J Geophys Res 100: 1981–2001

Isaak DG (1992) High-temperature elasticity of iron-bearing olivines. J Geophys Res 97: 1871–1885

Jackson I (2000) Laboratory measurements of seismic wave dispersion and attenuation: recent progress. In: Karato S et al (eds) Earth's deep interior: mineral physics and tomography from the atomic to the global scale. Geophysical Monograph 117, American Geophysical Union, Washington, DC, pp 265–289

Jackson I, Paterson MS (1987) Shear modulus and internal friction of calcite rocks at seismic frequencies: pressure, frequency and grain-size dependence. Phys Earth Planet Int 45: 349–367

Jackson I, Paterson MS (1993) A high-pressure, high-temperature apparatus for studies of seismic wave dispersion and attenuation. Pure Appl Geophys 141: 445–466

Jackson I, Rigden SM (1998) Composition and temperature of the Earth's mantle: seismological models interpreted through experimental studies of Earth materials. In: Jackson I (ed) The Earth's mantle: composition, structure and evolution, Cambridge University Press, New York, pp 405–460

Jackson I, Paterson MS, Fitz Gerald JD (1992) Seismic wave dispersion and attenuation in Åheim dunite: an experimental study. Geophys J Int 108: 517–534

Jackson I, Fitz Gerald JD, Kokkonen H (2000) High-temperature viscoelastic relaxation in iron and its implications for the shear modulus and attenuation of the Earth's inner core. J Geophys Res 105: 23 605–23 634

Jaoul O (1990) Multicomponent diffusion and creep in olivine. J Geophys Res 95: 17 631–17 642

Jin Q, Wilkinson DS, Weatherly GC (1998) Determination of grain-boundary film thickness by the Fresnel fringe-imaging technique. J Eur Ceram Soc 18: 2281–2286

Karato S, Jung H (1998) Water, partial melting and the origin of the seismic low-velocity and high-attenuation zone in the upper mantle. Earth Planet Sci Lett 157: 193–207

Karato S, Paterson MS, Fitz Gerald JD (1986) Rheology of synthetic olivine aggregates: influence of grain size and water. J Geophys Res 91: 8151–8176

Kohlstedt DL, Goetze C, Durham WB, Van der Sande J (1976) New technique for decorating dislocations in olivine. Science 191: 1045–1046

Li X, Romanowicz B (1996) Global mantle shear velocity model developed using nonlinear asymptotic coupling theory. J Geophys Res 101: 22 245–22 272

Minster JB, Anderson DL (1981) A model of dislocation-controlled rheology for the mantle. Phil Trans Roy Soc London 299: 319–356

Muan A, Osborn EF (1965) Phase equilibria among oxides in steelmaking. Addison-Wesley Publishing Company, Reading, Massachusetts, 236 pp

Nakamura A, Schmalzried H (1983) On the non-stoichiometry and point defects of olivine. Phys Chem Miner 10: 27–37

Nowick AS, Berry BS (1972) Anelastic relaxation in crystalline solids. Academic Press, New York, 677 pp

O'Neill HStC, Wall VJ (1987) The olivine-orthopyroxene-spinel oxygen geobarometer, the nickel precipitation curve, and the oxygen fugacity of the Earth's upper mantle. J Petrol 28: 1169–1191

Paterson MS (1990) Rock deformation experimentation. In: Duba AG, Durham WB, Handin JW, Wang HF (eds) The brittle-ductile transition in rocks. The Heard volume. Geophysical Monograph 56, American Geophysical Union, Washington, DC, pp 187–194
Poirier J-P (1985) Creep of crystals – high-temperature deformation processes in metals, ceramics and minerals. Cambridge University Press, Cambridge, 260 pp
Press WH, Flannery BP, Teukolsky SA, Vetterling WT (1986) Numerical recipes: the art of scientific computing. Cambridge University Press, Cambridge, 818 pp
Raj R (1975) Transient behavior of diffusion-induced creep and creep rupture. Metall Trans (A) 6: 1499–1509
Raj R, Ashby MF (1971) On grain boundary sliding and diffusional creep. Metall Trans 2: 1113–1127
Raterron P, Béjina F, Doukhan JC, Jaoul O, Liebermann RC (1998) Olivine/Fe-metal equilibrium under high pressure: an ATEM investigation. Phys Chem Miner 25: 485–493
Ritzwoller MH, Lavely EM (1995) Three-dimensional seismic models of the Earth's mantle. Rev Geophys 33: 1–66
Romanowicz B (1995) A global tomographic model of shear attenuation in the upper mantle. J Geophys Res 100: 12 375–12 394
Romanowicz B, Durek J (2000) Seismological constraints on attenuation in the Earth: a review. In: Karato S et al (eds) Earth's deep interior: mineral physics and tomography from the atomic to the global scale. American Geophysical Union, Washington, DC, pp 161–179
Rossman GR (1988) Vibrational spectroscopy of hydrous components. In: Hawthorne FC (ed) Spectroscopic methods in mineralogy and geology. Mineralogical Society America, Washington, DC, pp 183–206
Su W, Dziewonski AM (1997) Simultaneous inversion for 3-D variations in shear and bulk velocity in the mantle. Phys Earth Planet Int 100: 135–156
Su W, Woodward RL, Dziewonski AM (1994) Degree 12 model of shear velocity heterogeneity in the mantle. J Geophys Res 99: 6945–6980
Tan BH, Jackson I, Fitz Gerald JD (1997a) Shear wave dispersion and attenuation in fine-grained synthetic olivine aggregates: preliminary results. Geophys Res Lett 24: 1055–1058
Tan BH, Jackson I, Fitz Gerald JD (1997b) Grainsize dependence of solid state viscoelasticity in olivine aggregates. EOS (Trans Am Geophys Union) 78: (F)466
Thompson WK (1965) Infrared spectroscopic studies of aqueous systems I. Trans Faraday Soc 61: 1635–1640
Toomey DR, Wilcock WSD, Solomon SC, Hammond WC, Orcutt JA (1998) Mantle seismic structure beneath the MELT region of the East Pacific Rise and *P* and *S* wave tomography. Science 280: 1224–1227
van der Hilst RD, Kennett BLN, Shibutani T (1998) Upper mantle structure beneath Australia from portable array deployments. In: Braun J et al (eds) Structure and evolution of the Australian continent. American Geophysical Union, Washington, DC, pp 39–57
Vaughan PJ, Kohlstedt DL, Waff HS (1982) Distribution of the glass phase in hot-pressed, olivine basalt aggregates: an electron microscopy study. Contrib Min Petrol 81: 253–261
Webb SC, Forsyth DW (1998) Structure of the upper mantle under EPR from waveform inversion of regional events. Science 280: 1227–1229
Webb S, Jackson I, Fitz Gerald J (1999) Viscoelasticity of the titanate perovskites $CaTiO_3$ and $SrTiO_3$ at high temperature. Phys Earth Planet Int 115: 259–291
Zielhuis A, Nolet G (1994) Shear-wave velocity variations in the upper mantle beneath central Europe. Geophys J Int 117: 695–715

Appendix: Calculation of $G(\omega)$ and $Q^{-1}(\omega)$ from the parameters tabulated for the Andrade and generalised Burgers models

Application of the Boltzmann superposition principle to the case of sinusoidally time-varying stress $\sigma(t)$ and strain $\varepsilon(t)$ results in an expression for the dynamic compliance $J^*(\omega) = \varepsilon(t)/\sigma(t) = J_1(\omega) - iJ_2(\omega)$ that is the Laplace transform of the creep function $J(t)$ (e.g. Jackson 2000).

For the Andrade creep function (Eq. 1), the resulting expressions are

$$\begin{aligned} J_1(\omega) &= J_U + \beta\Gamma(1+n)\omega^{-n}\cos(n\pi/2) \text{ and} \\ J_2(\omega) &= \beta\Gamma(1+n)\omega^{-n}\sin(n\pi/2) + 1/\eta\omega \ , \end{aligned} \tag{A1}$$

where $\Gamma(1+n)$ is the gamma function.

For the generalised Burgers model (Eq. 2) the equivalent expressions are

$$\begin{aligned} J_1(\omega) &= J_U\left\{1 + \Delta\int_0^\infty D(\tau)\mathrm{d}\tau/(1+\omega^2\tau^2)\right\} \\ \text{and} \quad J_2(\omega) &= \omega J_U\Delta\int_0^\infty \tau D(\tau)\mathrm{d}\tau/(1+\omega^2\tau^2) + 1/\eta\omega \ , \end{aligned} \tag{A2}$$

with the distribution $D(\tau)$ of anelastic relaxation times given by Eq. (3).

From these expressions for $J_1(\omega)$ and $J_2(\omega)$, the frequency-dependent shear modulus

$$G(\omega) = [J_1^2(\omega) + J_2^2(\omega)]^{-1/2} \tag{A3}$$

and the associated strain energy dissipation

$$Q^{-1}(\omega) = J_2(\omega)/J_1(\omega) \tag{A4}$$

may be calculated.